Tectonics

RESEARCH ARTICLE
10.1029/2017TC004867

Key Points:
- We calculate 162 new focal mechanisms for the western and central Eastern Alps. Earthquakes and mechanisms only partially fit with mapped surface faults
- Stress orientation is deflected by 10–20° in a 70-km-wide zone around the boundaries of the Dolomites indenter
- Part of the Europe-Adria convergence is transferred to a 100-km-wide, seismically active thrusting zone 30 km north of the indenter corner

Supporting Information:
- Supporting Information S1
- Data Set S1
- Data Set S2
- Data Set S3
- Data Set S4
- Data Set S5
- Data Set S6
- Data Set S7
- Data Set S8

Correspondence to:
F. Reiter,
franz.reiter@uibk.ac.at

Citation:
Reiter, F., Freudenthaler, C., Hausmann, H., Ortner, H., Lenhardt, W., & Brandner, R. (2018). Active seismotectonic deformation in front of the Dolomites indenter, Eastern Alps. *Tectonics*, *37*, 4625–4654. https://doi.org/10.1029/2017TC004867

Received 13 NOV 2017
Accepted 9 NOV 2018
Accepted article online 12 NOV 2018
Published online 18 DEC 2018

Active Seismotectonic Deformation in Front of the Dolomites Indenter, Eastern Alps

F. Reiter[1], C. Freudenthaler[2], H. Hausmann[2], H. Ortner[1], W. Lenhardt[2], and R. Brandner[1]

[1]Institute for Geology, University of Innsbruck, Innsbruck, Austria, [2]Zentralanstalt für Meteorologie und Geodynamik, Vienna, Austria

Abstract We use earthquake focal mechanisms to study present-day deformation and stress in the western part of the Eastern European Alps. We define the following regions, based on seismicity and kinematically compatible focal mechanism types: (1) the northern and western parts of the Dolomites indenter, the western and central Tauern Window, and the northern Alpine margin and foreland lack significant seismicity. (2) The indenter boundaries are characterized by strike-slip faulting. Based on earthquake and geodetic data, the western and northern indenter boundaries are active sinistral and dextral strike-slip/oblique slip faults. (3) West and north of the indenter corner, we observe normal and strike-slip faulting in an up to 70 km-wide zone. From west to east, the minimum horizontal stress rotates clockwise about 10–20°, from NE to ENE. (4) North of (3), east of the Swiss/Austrian border, we find evidence for N to NNW directed thrust faulting, and local orogen-parallel extension. From our results and geodetic data, we infer that relative to a fixed northern foreland, NNW directed indentation is transferred at depth via the Sub-Tauern thrust system to this 100-km-wide zone of localized thrusting. A lack of evidence for major, active strike-slip faulting north of the Tauern Window is in line with geodetic data, which show no significant velocity difference between the northern part of the Eastern Alps and their foreland.

1. Introduction

Orogeny of the European Alps has been a long-lasting process, starting in the Cretaceous. In the Cenozoic, the European plate (Europe) collided with the Adriatic microplate (Adria; e.g., Dewey et al., 1973; Handy et al., 2010). The upper plate includes the Adria-derived Austroalpine and South Alpine units (Figure 1). A major role for the evolution of the Eastern Alps is attributed to the *South Alpine indenter* (e.g., Ratschbacher et al., 1991), a relatively rigid, less deformed piece of continental crust, which has been pushed into weaker parts of the orogen. Here we use the term *Dolomites indenter* (DI in Figure 1) for the northernmost part of Adria, which is delimited to the north by the Pustertal-Gailtal Fault (PGF) and to the west by the Giudicarie Fault (GF; Schmid et al., 1989). The two faults meet at almost right angle, at the northern corner of the indenter.

At its corner, the indenter comes very close to the Tauern Window (TW in Figure 1), an arcuate dome exposing oceanic remnants and units derived from the distal lower plate (e.g., Behrmann, 1988; Schmid et al., 2013; Selverstone, 1988). The Brenner Fault (BF) separates two areas of contrasting postcollisional deformation at the western boundary of the window. In the footwall of this west dipping low-angle normal fault, the Tauern units were folded and exhumed in Oligocene/Miocene times, during N-S shortening. A kilometer-thick mylonite zone with significant E-W stretching (Brenner shear zone, BSZ) forms the ductile portion of the fault. In contrast, the Austroalpine units in the hangingwall of the BSZ cooled below 300 °C in the Cretaceous (Fügenschuh et al., 1997) and remained in the field of brittle deformation since then. Shortening and exhumation within the TW can be linked to indentation and oblique lateral displacement along the indenter-bounding faults. East of the zone of maximum shortening, major parts of the Eastern Alps moved laterally in the Miocene (*lateral extrusion model*; Ratschbacher, Frisch, et al., 1991).

A shallow and moderate seismicity documents ongoing deformation north and west of the indenter (Figure 2). Here we use earthquake focal mechanisms to test to which extent present-day and Neogene tectonics are comparable. If so, we expect an influence of the indenter boundaries on faulting style and the stress field. For our study, we selected an area of 150 km width at both sides of the indenter corner, reaching 100 km to the north and 50 km to the south (Figure 1). In this area, focal mechanism and stress

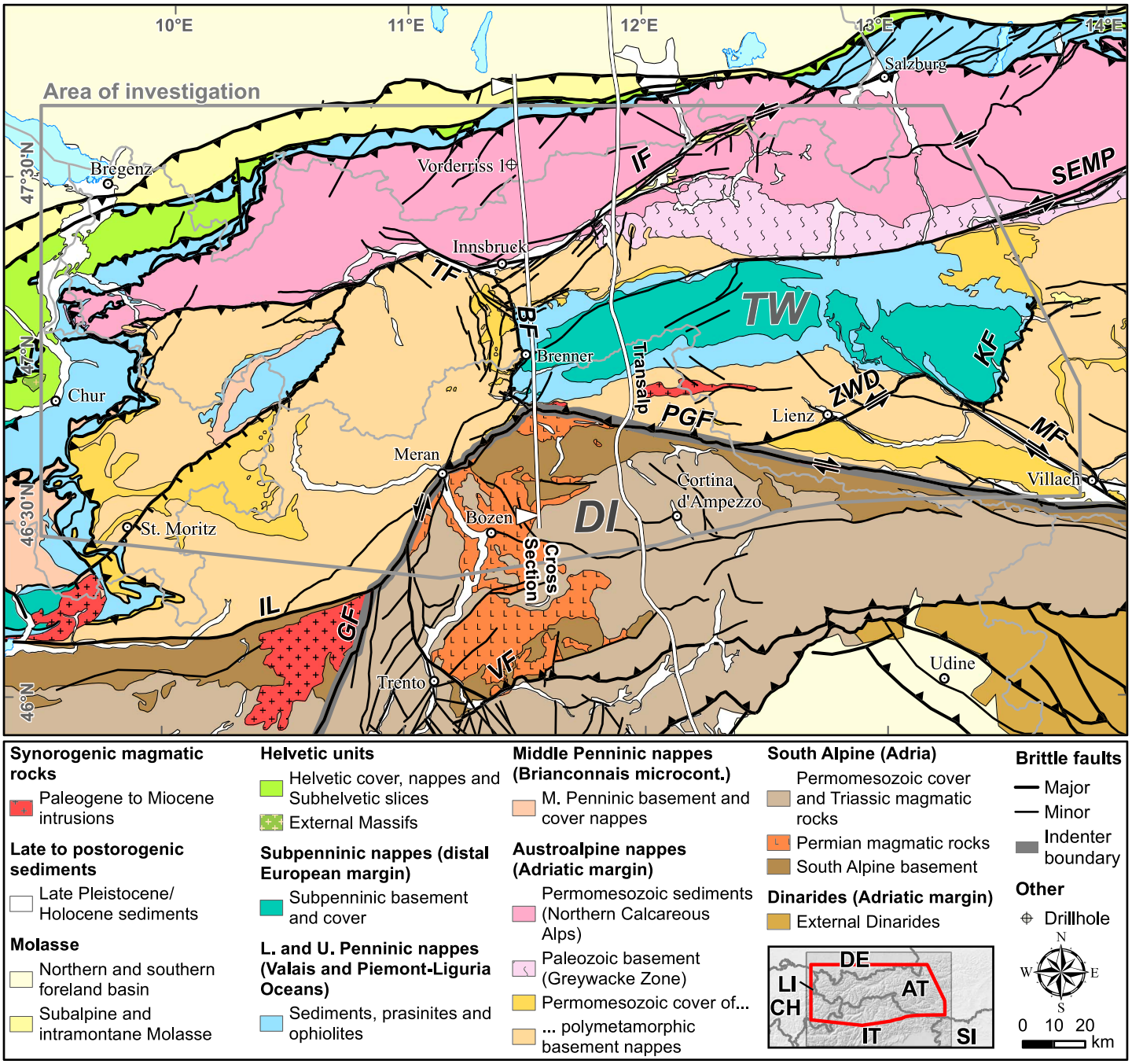

Figure 1. Tectonic map of the central Eastern Alps, showing important brittle faults active during late Alpine orogeny. Simplified from Brandner (1980b) and Bousquet et al. (2012), with supplementary information from Decker et al. (1994), Eisbacher and Brandner (1995), Ortner et al. (2015), Pomella et al. (2016), and published geologic and tectonic maps (Autonome Provinz Bozen, 2017; Bigi et al., 1990; Bundesamt für Landestopografie, 2005; Geologische Bundesanstalt, 2017a, 2017b). The Dolomites indenter (DI, the boundary is shown with a thick black line) is the South Alpine segment bounded by the Giudicarie Fault (GF) and the Pustertal-Gailtal Fault (PGF). The NNE striking GF and WNW striking PGF form a corner where they meet at the northernmost part of the indenter. At this corner, the indenter almost touches the Tauern Window (TW), a tectonic window, exposing units from below the Austroalpine nappe stack. Other major brittle faults labeled: BF Brenner Fault, KF Katschberg Fault, IF Inntal Fault, MF Mölltal Fault, SEMP Salzachtal-Ennstal-Mariazell-Puchberg Fault, IL Insubric Line, TF Telfs Transverse Fault, VF Valsugana Fault, ZWD Zwischenbergen-Wöllatratten-Drau Fault. Position of the drill hole Vorderriss 1 from Bachmann and Müller (1981). The cross section indicated is shown in Figure 8.

data are already available for the Swiss part and adjacent regions (see Kastrup et al., 2004; Marschall et al., 2013, and references therein). For the Austrian and Italian sectors, focal mechanisms are available only for some stronger events (e.g., Pondrelli et al., 2004; Slejko et al., 1987) and for earthquakes near the BF

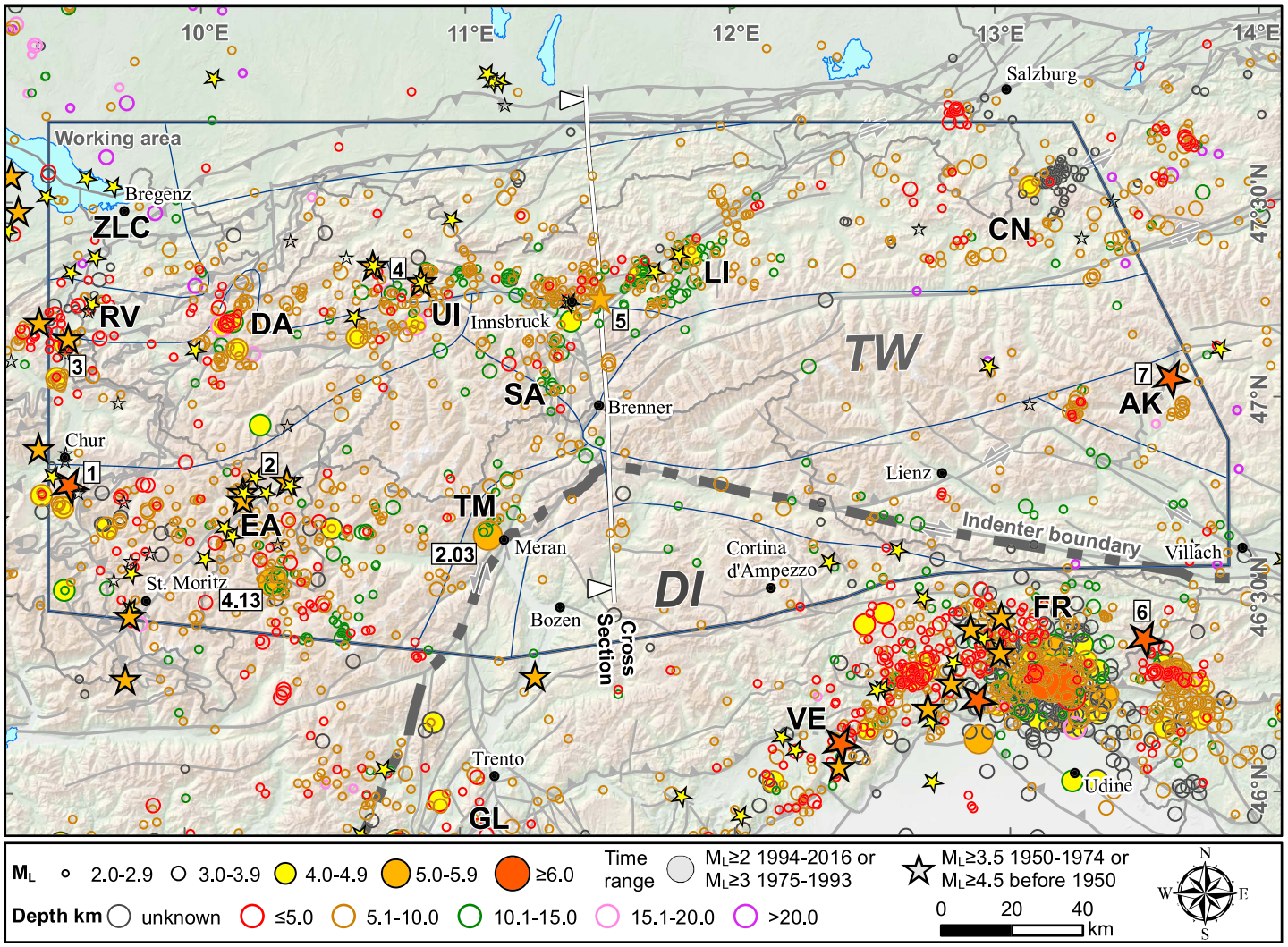

Figure 2. Distribution of instrumental and historical seismicity around the Dolomites indenter (DI) and the western termination of the Tauern Window (TW). Brittle faults as in Figure 1. Regions of enhanced seismicity are the Swiss/Austrian Rhine valley (RV), a NNE-SSW trending linear region between Davos and Arlberg (DA), Graubünden southeast of Chur, the Engadine and Ortler Alps (EA), the Upper Inn valley and adjacent northern areas (UI), the Lower Inn Valley (LI), and—outside of our study area—the Giudicarie-Lessini region (GL). Areas with lower but still elevated seismicity are the Texel Group and Meran-Passeier area (TM), the eastern Stubai Alps (SA), the central Northern Calcareous Alps (CN), and the Ankogel-Katschberg region (AK). The most prominent earthquake region shown on the map is the Friuli (FR)-eastern Veneto zone (VE), which is outside of our working area. Numbers refer to seismic events mentioned in the text. The thin, dark blue lines delineate seismotectonic domains we define below, in section 6.2. For contributing agencies to our earthquake catalog, see the section. Additionally, our earthquake catalog includes data from Schorn (1902), Förtsch and Schmedes (1976), Finetti et al. (1979), Galadini and Galli (1999), Poli et al. (2002), Ganas et al. (2008), and Hammerl (2017). The catalog is available as supporting Data Set S2. Digital elevation model from European Environment Agency (2013).

(F. Reiter et al., 2005). Recently installed seismic stations and the availability of data from temporary networks gave us the opportunity to investigate seismotectonic activity and the stress field in front of the indenter.

2. Tectonic Setting

2.1. The DI and Its Boundaries

Internal deformation of the DI is low in the northern and central western part (Castellarin et al., 1987; Castellarin & Cantelli, 2000). The southern sector is a Neogene to recent, foreland propagating fold-and-thrust belt (e.g., Caputo et al., 2010; Heberer et al., 2017; Nussbaum, 2000; Robl et al., 2017; Schönborn, 1999; Zattin et al., 2006). In the Veneto-Friuli area (VE and FR in Figure 2), thrusting has occurred since the Middle Miocene (Castellarin et al., 1987; Castellarin & Cantelli, 2000; Massari, 1990), probably decoupling the indenter from the

undeformed part of Adria (cf. Castellarin et al., 2006). Today, the southeastern DI is characterized by active S-SE directed thrusting, primarily at the extern-most thrust front (e.g., Benedetti et al., 2000). There, active crustal movements cause moderate to strong earthquakes (Figure 2; Basili et al., 2008; Burrato et al., 2008; Galadini et al., 2005; Pondrelli et al., 2001; Slejko et al., 1989). Compared to the central and northern indenter, its southwestern boundary (southern GF in Figure 1) is also seismically active, with strike-slip to oblique slip focal mechanisms. NW striking, dextral strike-slip faults link the GF to the active South Alpine thrust front in the Giudicarie-Lessini region (GL in Figure 2; e.g., Basili et al., 2008; Castellarin, Vai, et al., 2006; Viganò et al., 2008; Viganò et al., 2015).

The timing of the faults bordering the DI to the northwest and north constrains the age of indentation. They are part of the Periadriatic Fault (PF) that delimits the Southern Alps to the north (e.g., Schmid et al., 1989). Generally, the PF trends E-W, but the western indenter boundary is NNE-SSW oriented (Figure 1). There, the northern GF separates the ENE-striking Insubric Line from the ESE trending PGF (Figure 1; e.g., Pomella et al., 2011; Schmid et al., 1989; Viola et al., 2001). Rocks of the northern indenter exposed at the surface today had already reached a shallow level below zircon fission track (ZFT) closure prior to the onset of indentation (Pomella et al., 2012). Dextral semiductile movement on the Insubric Line, northern GF and PGF is synchronous to the emplacement of intrusives of Late Eocene/Lower Oligocene age (e.g., Blanckenburg et al., 1998; Hejl, 1997; Müller et al., 2001; Pomella et al., 2011; Schmid et al., 1987). Dating of fault gouges and pseudotachylites proves brittle movements at the GF and the structures linking the GF to the PGF in Oligocene/Miocene times. The faults moved with sinistral and northwest side up sense, as apatite fission track (AFT) ages indicate (Martin et al., 1998; Müller et al., 2001; Pleuger et al., 2012; Pomella et al., 2011, 2012). For the PGF, evidence for Miocene brittle, north side up, and dextral fault activity comes from tectonic analysis, ZFT and AFT cooling ages, and dating of fault gouges and pseudotachylites (Bartel et al., 2014; Läufer et al., 1997; Müller et al., 2001; Pomella et al., 2018; Rathore & Becke, 1980; Schmid et al., 1989; Sprenger & Heinisch, 1992; Zwingmann & Mancktelow, 2004). Austroalpine basement units next to the indenter, which are at the surface today, stayed near the brittle-ductile transition during indentation or had already cooled below the ZFT temperature before (e.g., Fügenschuh et al., 1997; Mancktelow et al., 2001; Pomella et al., 2011, 2012; Viola et al., 2001).

2.2. Orogenic Units North of the Indenter

Within the TW, Penninic and Europe-derived units from a structural position below the Austroalpine nappes are exposed at the surface (Figure 1; e.g., Schmid et al., 2013). Exhumation of the TW took place after the collision of Adria and Europe in Oligocene to Miocene times (Bertrand et al., 2017; Blanckenburg et al., 1989; Fügenschuh et al., 1997; Schneider et al., 2015). Doming of the window units was combined with orogen-parallel extension and indentation (e.g., Behrmann, 1988; Ratschbacher, Frisch, et al., 1991; Selverstone, 1988; see also the compilations of Rosenberg et al., 2018; Schmid et al., 2013). At the western termination of the window, the kilometer-thick BSZ indicates primarily ductile, top-to-the-west extension (Behrmann, 1988; Selverstone, 1988). The youngest AFT cooling ages from this area range between 4 and 7 Ma (Bertrand et al., 2017; Fügenschuh et al., 1997). The BSZ mylonites link to a sinistral shear zone at the NW corner of the TW (Töchterle et al., 2011).

Brittle fault studies from the TW confirm that orogen-parallel extension in the footwall of the BSZ/BF and sinistral shearing both reach into the brittle regime (Bertrand et al., 2015; Reicherter et al., 1993). Decker and Reiter (2003) report about systematically tilted, brittle normal faults on the northern and southern limbs of the westernmost Tauern antiform and hence infer post ZFT age doming. From 13 Ma onward, the westward dipping shear zone at the roof of the Penninic units had a brittle kinematic link out of the window, toward the Inn valley in the north, to the Inntal Fault (IF in Figure 1; Fügenschuh et al., 1997; Ortner et al., 2006). There, the BF separates basement units from each other, with similar ZFT ages but younger AFT ages in the footwall (Fügenschuh et al., 1997). In the hangingwall, synthetic and antithetic normal faults extend approximately 15 km west from the fault trace, with vertical displacements of up to several hundred meters. The strike of these faults follows the strike of the BF (e.g., Prager, 2003; Reiser, 2010; Rockenschaub et al., 2003). At its northern end, the BF is dissected by NW striking, steeply SW dipping normal faults and NW striking vertical, dextral strike-slip faults, which cut the ultracataclasites of the moderately dipping master fault (F. Reiter et al., 2007).

A southern continuation of the BF is not as straightforward as to the north. The fault can be traced to some kilometer south of the Brenner Pass (e.g., Agostinelli et al., 1995). A continuation from the TW to the PF can just be inferred. According to Behrmann (1988) and Fügenschuh et al. (1997), the BF should link along the Eisack Valley to the PGF. This is supported by Brandner et al. (2008), who describe brittle faults linking from the PGF to the TW. Selverstone (1988) inferred a continuation of the BSZ toward the GF. Rosenberg and Garcia (2011) link the BF the northern GF. This is supported by a westward continuation of young ZFT and AFT cooling ages (Middle and Upper Miocene, respectively) between the SW corner of the TW, the indenter and the northern GF (e.g., Pomella et al., 2012). Close to the northern DI boundary, brittle faults extend from the GF into the Austroalpine units (e.g., Luth et al., 2013; Viola et al., 2001). Mapping and brittle tectonic field studies revealed a zone of sinistral transpression near the GF and sinistral transtension to orogen-parallel extension close to the TW boundary (Luth et al., 2013; Spiess, 1995; Viola et al., 2001).

The eastern margin of the TW shows some similarities to the Brenner area, with the low-angle, southeast dipping Katschberg shear zone and the brittle Katschberg fault (KF in Figure 1; Genser & Neubauer, 1989; Scharf et al., 2013). This fault separates the Tauern units from the overlying Austroalpine. Both AFT and ZFT cooling ages jump across the fault (Hejl, 1997; Staufenberg, 1987; Wölfler et al., 2008), with youngest AFT ages of 3 Ma in the footwall (Bertrand et al., 2017).

2.3. Indentation/Lateral Extrusion Model

Several models have been developed to explain kinematic links between Dolomites indentation, Brenner and Katschberg shearing/faulting, and internal deformation of the TW (e.g., Frisch et al., 1998; Ratschbacher, Frisch, et al., 1991; Rosenberg et al., 2004). The models involve primarily N-NE directed movement of the indenter and shortening, exhumation, and stretching east of the BF. Austroalpine blocks north and east of the TW moved toward the east during lateral extrusion. These crustal wedges are separated from each other by conjugate sets of brittle, steeply dipping strike-slip faults. Sinistral faults limit these blocks in the north, the most important being the Salzachtal-Ennstal-Mariazell-Puchberg Fault (SEMP; Linzer et al., 2002; Rosenberg & Schneider, 2008; Töchterle et al., 2011; Wang & Neubauer, 1998). The BF and IF form the western and northern boundaries of the westernmost wedge (Figure 1; Ratschbacher et al., 1989). To the south, dextral strike-slip faults delimit the extrusion corridor. The most prominent ones are the PGF and the SE trending Mölltal fault (MF; Frisch et al., 2000; Kurz & Neubauer, 1996; Linzer et al., 2002; Ratschbacher et al., 1989).

3. Seismicity

Figure 2 shows selected epicenters in and around our working area, which is characterized by a weak to moderate seismicity. The northern boundary of the Alps, the TW and the northern and central western part of the DI show a remarkable low seismicity. The northern limit of the indenter cannot be recognized from the earthquake distribution (Figure 2). Since 1975, two earthquakes between local magnitude M_L 5 and 6 were registered in the area of investigation (numbers in parentheses refer to Figure 2): In 1999, a $M_L = 5.3$ event occurred in the Swiss/Italian Engadine Alps (4.13), and in 2001 an earthquake of the same magnitude close to Meran (2.03). The instrumental record contains 16 events between $4 < M_L < 5$ for the same time span. Moderate to strong historical seismicity is also known. A $M_L = 6.5$ event occurred in 1295 at the western end of the Engadine Alps (1) and three events of $M_L = 5$ in 1503, 1813, and 1961 in their center (2). The Rhine Valley at the Swiss/Liechtenstein border holds one $M_L = 5$ event from 1681 (3) (all Schweizerischer Erdbebendienst, 2010). Two earthquakes of $M_L = 5.1$ and 5.3 stroke the region north of the Upper Inn Valley in 1886 and 1930 (4). In 1670, a magnitude 5.2 event hit the Lower Inn Valley (5). A catastrophic event of $M_L = 6.8$ occurred in the region Villach-Friuli in 1348, possibly outside of our study area (6). The Katschberg region, besides a low recent seismic activity, is the source of a significant historic earthquake in 1201 (7), estimated to $M_L = 6.1$ (all Zentralanstalt für Meteorologie und Geophysik, 2016).

In terms of hypocentral depth, all earthquakes lie in the shallow range (Figure 2). Since the earthquake catalog comprises a long time range and our research area is covered by different seismological services, location algorithms and velocity models used are not consistent. Furthermore, the accuracy of the depth determination varies significantly due to the heterogeneous density of the seismic network (Figure 3). Microseismically determined depths are routinely crosschecked with macroseismic depths if available for

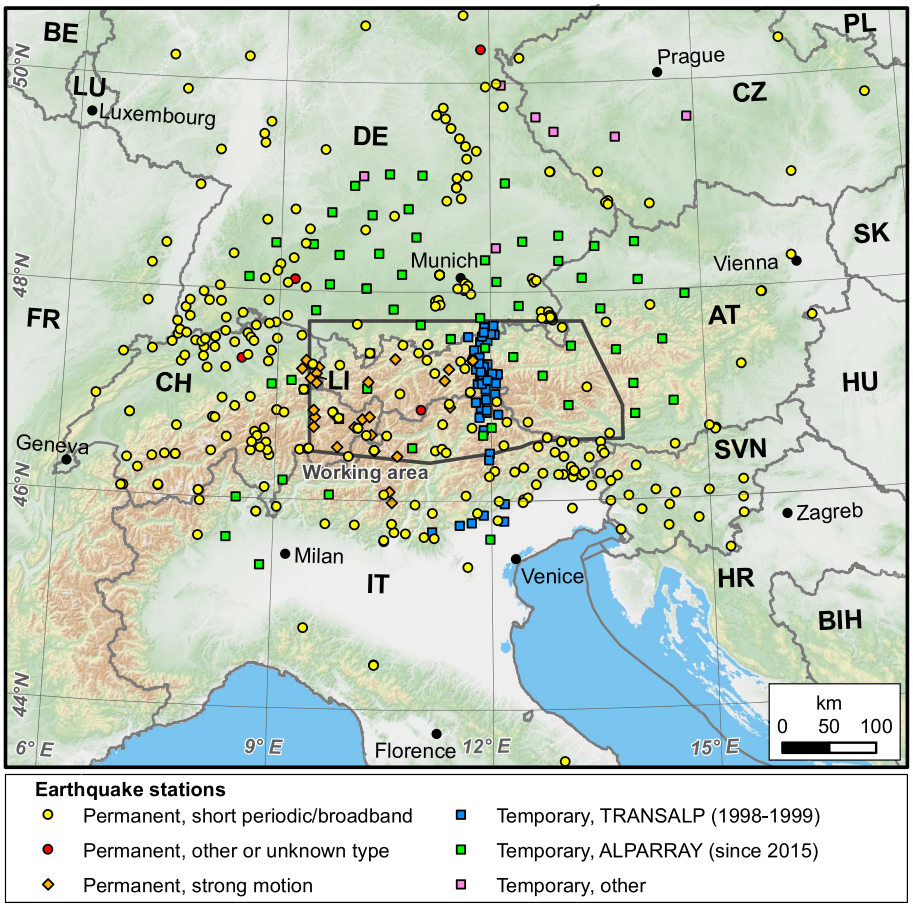

Figure 3. Earthquake stations of which digital waveforms or bulletin data (International Seismological Centre, 2017) were used for this study. For contributing agencies, see the section. The station list is available as digital Data Set S3. Digital elevation model from European Environment Agency (2013).

the Austrian catalog (cf. Lenhardt et al., 2007). We applied the depth subdivision shown in Figure 2 only to events from 1975 onward and generally excluded earthquakes with $M_L < 2$. Based on the study of Lenhardt et al. (2007), we estimate the depth error for the events shown to be smaller than 3 km. In areas with a dense station coverage, the depth error is better than 1 km. Despite all location uncertainties, a majority of hypocenters is located between 5 and 15 km. An exception is the NW corner of our research area, where events extend down to 20–30 km, a phenomenon known as *zone of lower crustal seismicity* (LCS in Figure 2; see Singer et al., 2014 and references therein).

4. Data Acquisition and Processing

4.1. Station Network

National seismic services have successively densified and digitized their station networks during the period of investigation, which mainly comprises the digital era. The permanent networks allowed obtaining successful focal mechanism calculations for events of $M_L \geq 3$ at the beginning of a reasonable digital network/data coverage (1996), while near present we were able to solve most events for $M_L \geq 2.5$, depending on the location of the epicenter in relation to the network. The map in Figure 3 shows all stations used for the present study. Permanent networks providing public waveform data are mentioned in the section. In addition, we used waveforms from the Seismological Service of Austria (ZAMG), from Diehl et al. (2009), from the temporary TRANSALP network, and from the ongoing AlpArray program (AlpArray Working Group, 2015).

4.2. Event Selection, Waveform Retrieval, and Signal Processing

We searched the compiled earthquake catalog for events of $M_L \geq 2.5$ in the area of interest. Additionally, we recalculated some published mechanisms when the full station coverage had not been used for an existing calculation. For main and aftershock sequences, we did not calculate fault plane solutions for all aftershocks if their magnitude was below 3.

We worked with ObsPy, a python-based seismology script package (Beyreuther et al., 2010) to retrieve waveform data from the European Integrated Data Archive (EIDA). For older events and nonpublic ZAMG stations, these data were obtained on file from the ZAMG data center. For events before 2016, we retrieved waveform data from the OGS network via their OASIS web interface (Istituto Nazionale di Oceanografia e di Geofisica sperimentale, 2013). For data processing and visualization, we used the freeware SeisGram2K, Version 7.0.0X10 (Lomax, 2016).

If possible, we picked the desired onset from the unfiltered trace. If the waveform was superimposed by noise or a high-frequency signal, we applied a baseline correction followed by a band-pass filter 1–30 Hz or 1–10 Hz. We used a Butterworth-type filter (frequency response as flat as possible in the passband; Butterworth, 1930) with two poles (for 1- to 10-Hz band with four poles) to avoid acausal distortion, despite the small phase shift introduced to the trace. All amplitudes were measured peak to peak, after 1- to 30-Hz band-pass filtering.

5. Calculation Methods

5.1. Event Relocation

We applied the probabilistic earthquake location method NonLinLoc (Lomax et al., 2000). For relocation we used a 3-D velocity model derived from CELEBRATION 2000 and ALP2002 data (Behm, 2009; Behm et al., 2007), extended to the west using the model of Waldhauser et al. (2002). To assess absolute location uncertainties, we investigated events from two quarries within and two outside of the study area (eastern Austria) and events from a recent earthquake series.

First, we inspected 308 mine blasts with median values of their magnitudes within $0.7 < M_L < 1.2$. Only 16 blasts fulfilled the 95 % *ground truth 5 km criteria* (GT5; Bondár et al., 2004). The mean horizontal location error for these quarries is between 1.6 and 2.6 km (relocations) and between 1.5 and 2.8 km (ZAMG routine). Focal depths have median values between −0.7 and 2.5 km (relocations) and were fixed to 0 km in the routine ZAMG location. We computed the distance within 95% of the events were located. Resulting values are between 3.2 and 5.8 km for relocations and between 3.1 and 6.1 km for routine ZAMG location. This shows that even locations of small magnitude are consistently precise when using the 3-D model.

Second, we relocated an earthquake series close to Innsbruck, which had a main shock with $M_L = 3.8$. Out of 229 events, 18 complied with the GT5 criteria. Relative uncertainty was calculated by the average difference to the geometric mean location of the series. The estimated relative epicenter errors are ±1.8 km (relocations) and ±1.3 km (ZAMG routine) for poorly constrained events and ±1.0 km (relocations) and ±1.2 km (ZAMG routine) for events fulfilling the GT5 criteria.

5.2. Fault Plane Solutions

5.2.1. Principle

Earthquakes originating from slip on a fault generate a characteristic body wave radiation pattern (e.g., Byerly, 1955). The polarity of the *P* and *S* wave onsets and their amplitude ratios can be used to reconstruct geometry and relative movement of the fault causing a seismic event (e.g., Snoke, 1989). A restriction of this method is the symmetry of the radiated body waves. The fault plane solution yields two nodal planes perpendicular to each other, with opposite movement sense. Without further knowledge (e.g., from aftershock studies), it remains open, which of the planes slipped.

5.2.2. Velocity Model

To calculate the takeoff and incidence angles of the *P* and *S* arrivals, we adapted the 1-D AK135 velocity model above the Moho discontinuity (Kennett et al., 1995), with continuously increasing *P* and *S* wave velocities and density. The details of the model are shown in supporting Data Sets S1 and S5. The depth of the Moho was set to 45 km, a reasonable mean value for the study area, obtained from the TRANSALP campaign

and recent seismic tomography results (Behm, 2009; Kummerow et al., 2004; Lüschen et al., 2006; Waldhauser et al., 2002). We accounted for station altitude in angular calculations.

5.2.3. Body Wave Polarities and Amplitude Ratios

After signal processing, we rotated all traces about the *z* axis into the event-station azimuth. We picked the polarity of the *P* wave and the radial component of the *S* wave onset (*SV*) on the *Z* trace. The polarity of the transverse component of the *S* wave onset (*SH*) was picked on the rotated *E* trace. Each polarity reading was assigned a quality between 1 (*excellent*) and 4 (*speculative*), see supporting Data Set S1 for details. *SV* and *SH* onsets were only picked if they were not obscured by other arrivals. We additionally used polarity readings contained in the ISC seismic bulletins for some events before the year 2000 (International Seismological Centre, 2017). For those cases, the quality of the polarity reading was set to 0 (*not recorded*).

Amplitudes of the body wave onsets were measured from the integrated and rotated *Z* and *E* traces. The software *FPS*, version 4 F. (Reiter & Lenhardt, 2006, 2017), corrects free-surface effects with the code of Snoke (2003), after the formulation of Aki and Richards (2002). Amplitude ratios containing SV were not calculated when the angle of emergence for a station was closer than 5° to the critical angle (Evans, 1984). We did not apply a correction for attenuation, since sample calculations have shown that amplitude ratios do not substantially change.

5.2.4. Calculation and Visualization

We calculated all focal mechanisms with the software *FocMec* (Snoke, 2003). FocMec allows the usage of first onset polarities of *P*, *SV*, and *SH* waves as well as amplitude ratios involving *P*, *SV*, and *SH*. FPS acts as a graphical interface between the database holding all numerical values and the FocMec software and for data preparation. The software is able to visualize *P* and *S* wave onsets differentiated by quality classes, as well as amplitude ratios, and their predicted values for a focal mechanism calculated with FocMec. A visual check of predicted *SH* and *SV* wave polarities is implemented, using the code of Frohlich (1996).

We used the most sensitive setting of FocMec for calculation, with a one-degree step of the search angle. Since amplitude ratios cover a wide range, FocMec treats their values in $\log_{10}$ scale. The limit for amplitude errors was set to $10^{0.5}$ for all calculations. We did not apply any weighting of near-nodal stations.

In most cases, one or more polarity errors occurred in the data set; that is, the measured and predicted polarities were opposite to each other. During calculation, we stepwise increased the number of allowed polarity errors until a valid fault plane solution could be obtained. The result was then further refined in three stages: (1) avoid errors for polarity picks with a high quality ranking, (2) narrow the number of valid results by minimizing the amount of amplitude errors, and (3) from the remaining set of solutions manually select the mean orientation of nodal planes. For most events, we could calculate mechanisms without polarity errors of excellent polarity rating. The datasheets in the supporting information S1 document all results and errors graphically and in tabular form, separated for pick quality classes.

We manually assigned a quality class Q between 1 (*reliable*) and 4 (*speculative*) to our fault plane solutions. Q depends on the angular scattering of valid solutions and the stability of the result if one or more station readings close to the nodular planes are skipped (geometric stability test). Additionally, we considered the number of station readings available and with contradicting polarity. The criteria are listed at the end of the datasheets S1. Besides the quality factor, we show all readings with their pick quality and the geometric spread including all valid fault plane solutions in Table S1 and Data Set S1.

5.3. Stress Analysis

A common stress tensor can be calculated from a set of focal mechanisms that origin from a uniform stress field, comparable to the derivation of a stress tensor from slickensides in brittle microtectonics (e.g., Angelier, 1979). Because of the ambiguity of mechanisms, inversion methods need to select one of the two nodal planes available (e.g., Gephart, 1990; Gephart & Forsyth, 1984; Lund & Slunga, 1999; Lund & Townend, 2007; Michael, 1987; Vavryčuk, 2014) or need to find an algorithm to overcome the double-couple problem (e.g., Angelier, 2002).

We defined seismotectonic domains/subdomains (see results and discussion for details) according to mechanism types and their spatial distribution. All mechanisms within one subdomain were taken to compute a best fit stress orientation. For calculation, we used the Matlab script *Stressinverse* (*SI*; Vavryčuk, 2014). The script is based on the least squares inversion method of Michael (1984), which is iteratively applied

on the data set. SI takes care of a fault instability constraint after Lund and Slunga (1999). An additional result is the selection of one out of the two nodal planes based on the instability criterion, for a given friction and stress ratio. To illustrate the confidence of the result, the orientations of the focal planes are superimposed with random noise (100 variations, standard deviation of 5°). Since SI yields a friction coefficient μ, which results in the highest overall instability, we could also calculate the angle

$$\alpha = 45 - \frac{\tan^{-1}\mu}{2} \; [^{\circ}], \tag{1}$$

a relationship derived from the Mohr circle. In the plane defined by the fault normal and the slip lineation, α is measured between the maximum shear stress and the fault slip.

We calculated a second inversion on all data sets with the method of Gephart and Forsyth (1984), later referred to as *GF*. We used the software FMSI (Gephart, 1990), applying the exact mode. We did not specify a preferred fault from the two nodal planes and selected σ_1 as the primary stress direction except for domain 6, where we selected σ_3. To start search, we set the orientation of the stress axes to the values derived from the SI calculation. The variance of the σ_1 and σ_3 stress directions was set to 40°; we chose a 5° search grid. The shape ratio R (see equation (3) for definition) should be searched between 0 and 1 in steps of 0.05.

We crosschecked the results with the *numerical method for dynamic analysis of calcite twin lamellae* (*NDA*; Spang, 1972). This method calculates incremental strain and takes the angle α between maximum shear stress and the fault slip as input parameter. We set α = 45°. This assures equal results independent of which of the two nodal planes is selected as input. The calculation was performed with the software *TectonicsFP* (Ortner et al., 2002) where a code of Sperner and Ratschbacher (1994) of Spang's method is available for brittle fault analysis. We treat stress and strain ratios of the two methods equally, being aware of the limitations especially for the orientation of the strain axes (cf. Célérier et al., 2012; Twiss & Unruh, 1998). To distinguish the results of the NDA method from the stress calculations, we use the symbol λ for strain instead of σ for stress. For map display, the orientations of σ_1 and σ_3 (λ_1 and λ_3) were transformed to azimuths of maximum and minimum horizontal stress σ_H and σ_h (λ_H and λ_h), using the script of Lund and Townend (2007), which is implemented in the MSATSI code of Martínez-Garzón et al. (2014).

To compare the results and for tectonic interpretation, we used the stress, respectively, strain ratio (Angelier, 1979; Bott, 1959), which beside the orientation of the principal axes is an output of all three inversion methods:

$$\varphi = \frac{\sigma_2 - \sigma_3}{\sigma_1 - \sigma_3} \text{ for } \sigma_1 > \sigma_2 > \sigma_3 \text{ (compressive stresses positive; use } \lambda \text{ instead of } \sigma \text{ for NDA)} \tag{2}$$

The shape ratio given by the SI script is calculated after Gephart and Forsyth (1984) and equals

$$R = 1 - \varphi \tag{3}$$

We used φ together with the distribution of the PT axes to derive the principal tectonic regime (e.g., Célérier, 1995; Lavenu & Cembrano, 1999; Meschede, 1994; Ritz & Taboada, 1993).

With the strain tensor derived from the NDA inversion, we finally checked the focal mechanisms for their kinematic compatibility. With the TectonicsFP software, we tested if the calculated stress vector (stress acting on the nodal planes) imposes the observed slip (calculation from Sperner et al., 1993). If the calculated slip was opposite to the observed, the focal mechanism was marked with *nev* (Groshong, 1974).

6. Results

6.1. Relocation

The main reason for the 3-D relocation was to prove if the focal depths and the locations have been well constrained by the routine ZAMG location procedure and if the complex velocity structure of the Eastern Alps affects these results used for interpretation in this work. For all events selected for focal mechanism calculation, we started with the coordinates provided by the national or regional permanent network. ZAMG routinely locates with a 1-D-velocity model IASP91 approach, while the Swiss Seismological Service has been using a 3-D Grid search method for more than 10 years (Deichmann et al., 2006). If an event had

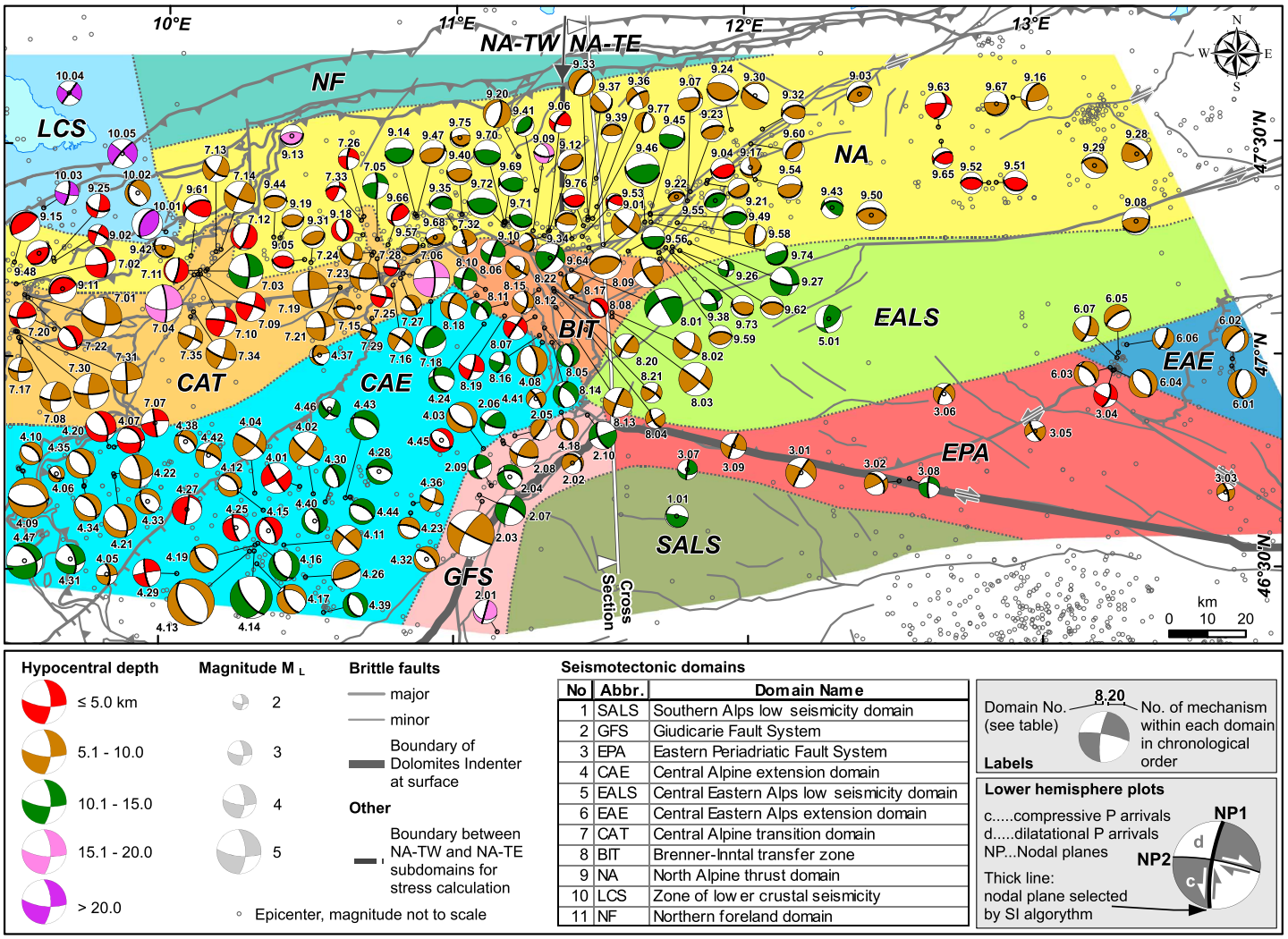

Figure 4. Map showing the results of new together with published focal mechanisms and waveform inversions of Baer et al. (2001), Baer et al. (2007), Baer et al. (2005), Bernardi et al. (2005), Braunmiller et al. (2002), Deichmann et al. (2002), Deichmann et al. (2006), Deichmann et al. (2010), Deichmann et al. (2011, 2012), Diehl et al. (2014), Diehl et al. (2013), Istituto Nazionale di Geofisica e Vulcanologia (2017), Kastrup et al. (2004), Kraft (1999), Marschall et al. (2013), Pondrelli et al. (2004), Pondrelli et al. (2002), F. Reiter et al. (2005), Roth et al. (1992), Saint Louis University Earthquake Center (2017), Schweizerischer Erdbebendienst (2017), Slejko et al. (1989), Slejko and Rebez (1988), and Viganò et al. (2008). We grouped the mechanisms into 11 seismotectonic domains (see text). The numbers given to each diagram correspond to Figure S1 and Table S1. These domains of active seismotectonic deformation are only partially consistent with surface geology but give an insight into active orogenic processes at the western margin of the Eastern Alps. Colored lower hemisphere diagrams were drawn with Esri™ ArcMap 10.5 and python™ script from Wu (2016). The inset on the lower right explains the diagrams used, a more detailed description is given in Figure S2.

already been 3-D located and published, we used this location and cite the source in Table S1. For the remaining events that were covered by our velocity model and match the GT5 criteria, we calculated a 3-D relocation. Out of 162 events, 153 had a 1-D model-derived location. We relocated a subset of 70 out of those.

P and *S* wave arrivals from stations within a radius of 150 km around the event were used for the 3-D grid search algorithm. Six of the recalculations delivered negative *z* coordinates; we fixed their depth to 2 km. To document our relocations, we investigated the differences between routine ZAMG locations and the probabilistic method and assessed location uncertainties. For focal depth differences, there is obviously no trend with the number of observations, which ranges between 16 and 58. The average *z* differences of 1.7 ± 3.5 km (instrumental data) and 0.6 ± 2.9 km (macroseismic evaluation) show that 3-D locations are slightly shallower than the 1-D routine locations, an effect also observed by Husen et al. (2003). Relocated focal depths are in better agreement with depths derived from macroseismic evaluations. The latitude and longitude differences average at 0.2 ± 1.1 km and 0.8 ± 1.2 km, respectively. The standard errors ERH and ERZ (Lee & Lahr, 1975;

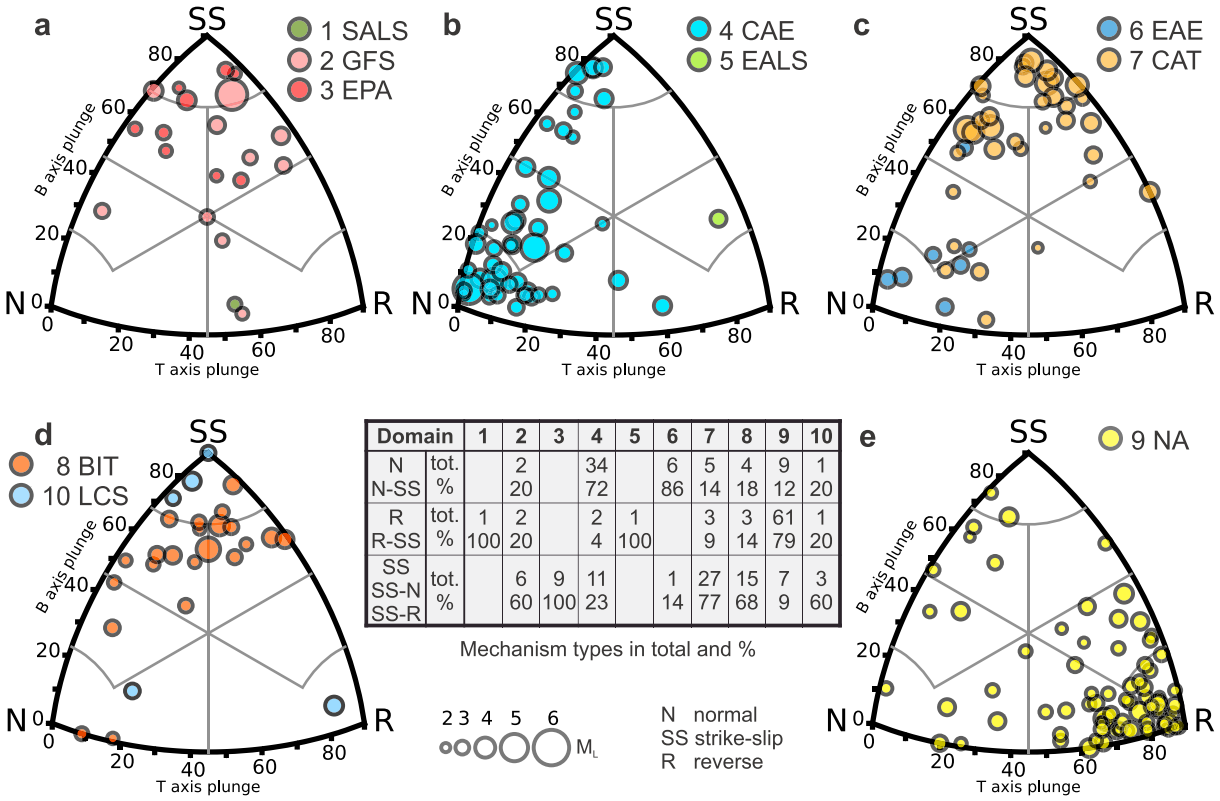

Domain		1	2	3	4	5	6	7	8	9	10
N	tot.		2		34		6	5	4	9	1
N-SS	%		20		72		86	14	18	12	20
R	tot.	1	2		2	1		3	3	61	1
R-SS	%	100	20		4	100		9	14	79	20
SS	tot.		6	9	11		1	27	15	7	3
SS-N			60	100	23		14	77	68	9	60
SS-R	%										

Figure 5. Ternary diagrams, plotting the plunge of the intermediate (B) and tension axes (T) of focal mechanisms to illustrate the faulting style of the seismotectonic regimes. The points are scaled by magnitude. Point colors correspond to domain colors on the maps in Figures 4, 7 and 9a. Plotting method modified after Kaverina et al. (1996), calculated with FMC script (Álvarez-Gómez, 2014). The seismotectonic domains are explained in the text. Note that the ternary diagrams do not reflect fault orientation, which is an additional criterion for the delineation of the seismotectonic domains.

Lomax et al., 2000) are shown on the calculation data sheets in supporting Data Set S1. All relocation parameters and results are listed in Data Set S4.

6.2. Focal Mechanisms

6.2.1. Faulting Style and Seismotectonic Domains

We were able to calculate 162 geometrically unambiguous fault plane solutions. Supporting Table S1 and Data Set S6 list basic event data, the orientation of the nodal planes, and the principal axes for our results together with 52 published focal mechanisms we considered. In the central and eastern working area, we excluded published events with $M_L < 3.5$ for years 1990 and before and generally excluded events before 1980. Those can be found in the compilations of Slejko et al. (1989), and Reinecker and Lenhardt (1999). Figure S1 illustrates the results and lists additional numerical parameters like the number of polarities used in total and with opposite polarity than predicted, the RMS error and the number of amplitude ratios in total and above the error limit. Lower hemisphere diagrams in Figure S1 show the maximum spread of valid solutions without further refinement by amplitude ratios. All detailed results and input parameters are illustrated in the supporting Data Sets S1 and S7.

Based on epicenter distribution, focal depths, and mechanisms (fault type and orientation), we divided our research area into 11 seismotectonic domains, explained below in detail. Except in domain LCS, almost all events occurred in a depth interval between 3 and 15 km. Within each of those domains, we could not observe a significant variation in mechanism type or orientation, depending on focal depth. Considering this and the location errors (cf. Data Set S4), we did not further subdivide the domains vertically. Figure 4 shows the entire working area with our results, for detail maps see Figures S3 to S7. The focal mechanisms include all principal fault types and transitions in between them: 61 normal faults, of which 19 show a transition to strike-slip; 71 reverse faults of which 12 show a transition to strike-slip and 82 strike-slip faults of which 31 show a transition to normal and 21 to reverse faulting (Table S1). Figure 5 illustrates different mechanism types found

in the various domains in a ternary diagram, based on the orientation of their PT axes. In the following chapters, we describe the regional distribution of the results. We start with the indenter and explain the defined zones from south to north, with increasing indenter distance.

6.2.2. The Indenter and Its Boundaries

1. *Southern Alps low seismicity domain* (SALS): The northwestern indenter area is characterized by a low seismicity. No earthquakes with $M_L > 4$ are known, and epicenters appear to be spatially distributed and not aligned along a specific lineament or structure. Hypocentral depths range from 5 to 15 km (Figure 2). We calculated one focal mechanism, a reverse fault indicating NNE-SSW shortening (Figures 4, 5a, and S3).
2. *Giudicarie Fault System* (GFS): Near the GF, mainly outside the DI boundary, we observed a slightly elevated seismicity, compared to domain SALS. Hypocenters are located between 5- and 15-km depth (Figure 2). We could solve 10 fault plane solutions and obtained strike-slip mechanisms with transitions to normal and reverse faulting (Figures 4, 5a, and S3). In most cases, one nodal plane is oriented parallel to the mapped GF. The strike of these nodal planes follows the curvature of the indenter boundary at the northern corner. This domain also holds one of the strongest events with an available mechanism, the 2001 Meran earthquake of $M_L = 5.3$ (event 2.03; Pondrelli et al., 2004).
3. *Eastern Periadriatic Fault System* (EPA): The area between the TW and the PGF is characterized by a low seismicity. Most events are located in the depth interval between 5 and 15 km (Figure 2). Epicenters generally do not align along the PGF, but four events suitable for focal mechanism calculation do so. We computed exclusively strike-slip mechanisms, with one nodal plane being parallel to the strike of the PGF, or, at the eastern limit of EPA, parallel to the MF trend (Figures 4, 5a, and S3).

6.2.3. Extension and Strike-Slip Faulting West, North, and East of the Indenter Corner

4. *Central Alpine extension domain* (CAE): The region west and north of the GFS is characterized by normal faulting with slip directions at an acute angle and parallel to Giudicarie strike, and subordinate oblique/strike-slip faulting on NE and NW striking planes. Hypocentral depths range from shallower than 5 to 15 km, with a maximum in the 5- to 10-km interval (Figure 2). The zone can be traced from the southwestern corner of our working area where most events cluster (Engadine Alps-St. Moritz-Chur) to the southwestern tip of the TW. This domain contains one of the strongest earthquakes from our instrumental data set, a normal faulting event with $M_L = 5.3$ (event 4.13). As in domain GFS, the orientation of faults changes slightly north of the indenter corner, so that fault strike is nearly perpendicular to the strike of the adjacent indenter boundary. The boundary to domain GFS is sharp, with a lack of normal faults there (Figures 4, 5b, and S4).
5. *Central Eastern Alps low seismicity domain* (EALS): This zone with very little seismotectonic deformation comprises mainly the TW except its northwest and southeast corner. Our catalog holds only 16 earthquakes in domain EALS. Most hypocenters were located between 5- and 10-km depth (Figure 2). We could calculate one fault plane solution, an oblique reverse fault indicating NW-SE directed shortening (Figures 4, 5b, and S5).
6. *Central Eastern Alps extension domain* (EAE) The southeastern corner of the TW and its surroundings are dominated by active extension in ENE to SE direction. A great majority of hypocenters is located between 5- and 10-km depth (Figure 2). The quality of fault plane solutions in this domain is worse compared to areas west and north of the indenter because of an unfavorable station geometry and weak onsets for most events and stations. We set the boundary to neighboring domain EPA to the switch from normal to strike-slip faulting (Figures 4, 5c, and S5).

6.2.4. Transitional Domains Between the Indenter and the Northern Alps

7. *Central Alpine transition domain* (CAT): This zone is located between domain CAE framing the DI in the northwest and the northern Alps (domain NA, see below). Epicenters cluster in the central northern, northwestern, and northeastern sector of the domain. Hypocenters lie between 2- and 10-km depth (Figure 2). Strike-slip faulting dominates, but occasional reverse and normal mode focal solutions exist. Most nodal planes strike W to WSW and N to NNW, hence show a small but evident counterclockwise rotation compared to neighboring domains CAE and BIT where strike-slip faults commonly strike NW and NE. We extended domain CAT to the north into domain NA along two N to NNE striking zones, characterized by strike-slip faulting, one nodal plane being parallel to each zone boundary (Figures 4, 5c, and S6).
8. *Brenner-Inntal transfer zone* (BIT): This region has a higher seismicity than domain CAT. Event depths range mostly between 5 and 15 km (Figure 2). Strike-slip and oblique-slip faulting dominates the focal mechanisms, superimposed by normal and oblique normal faulting. For strike-slip mechanisms, one of the nodal

planes commonly strikes parallel or oblique to the IF, the second plane parallel to the TF (cf. Figure 1). The strike of normal faults is at right angle to the strike of the GF-PGF transition at the nearby indenter corner. We set the diffuse boundary to domain CAE with the predominance of strike-slip faulting over normal faulting (Figures 4, 5d, and S6).

6.2.5. The Northern Sector of the Eastern Alps

9. *North Alpine thrust domain* (NA): The northernmost region of the orogen shows a majority of N-S shortening reverse faults with transitions to strike-slip faulting. Within NA, seismicity increases from north to south. The area around and the Inn Valley east of Innsbruck (cf. Figure 2) exhibit a comparable high seismicity. While hypocentral depths range between 2 and 15 km, with a maximum between 5 and 10 km, the lower boundary of the seismogenic zone deepens with increasing distance from the north Alpine thrust front and along the Inn Valley east of Innsbruck, from east to west (Figure 2; F. Reiter et al., 2003). Locally, we found normal faults with ENE to NE directed extension and single strike-slip mechanisms indicating N-S shortening. In many cases, the dip of south facing nodal planes is lower than the dip of the north facing conjugate. The boundary to domains CAT and BIT is rather sharp, with a switch from thrust to strike-slip faulting. The boundary to domain EALS follows the western continuation of the SEMP, where seismicity rapidly decreases. The SEMP segment in our working area (cf. Figure 1) is neither visible with a concentrated seismicity nor with strike-slip mechanisms. The Inn Valley east of Innsbruck and the associated IF (Figure 1) cross domain NA diagonally (Figures 4, 5e, and S7). However, only close to Innsbruck, we obtained one strike-slip fault plane solution (9.01). At the western end of our working area, domain NA pinches out near the Swiss/Austrian Rhine valley, where strike-slip focal mechanisms predominate over thrust events (cf. Kastrup et al., 2004; Marschall et al., 2013).
10. *Zone of LCS*: At the northwestern corner of our research area, we observed a region, where the epicentral depth distribution shows two peaks, at 5–10 and 30–35 km (Figure 2). We found three strike-slip focal mechanisms, and one thrust mechanism indicating N to NW shortening within the lower crust of Europe. One normal mechanism with orogen-parallel extension is located in the Alpine nappe stack. We set the boundary to the neighboring domains with the onset of the lower crustal events (Figures 4, 5d, and S7). The zone continues further west and widens north of the Alpine front, outside of our working area. There, Deichmann (1992) and Singer et al. (2014) also described a combination of strike-slip and normal events.
11. *Northern foreland domain* (NF): The area north of the basal thrust of the Northern Calcareous Alps (NCA) is characterized by a very low seismicity (Figures 1, 2, 4, and S7). No fault plane solution could be calculated.

6.3. Stress Analysis

6.3.1. General Results

Domains SALS, EALS, and NF yielded no or too less fault plane solutions for stress calculations. Due to the small number of input data, results for domain LCS must be regarded as preliminary. As pointed out above, within the remaining domains we could not find an obvious relation between mechanisms and focal depth. Considering the number of solutions and the variation in mechanism types and their orientation, we did not further subdivide the seismotectonic domains for stress calculation and used all mechanisms within each domain to retrieve information about the stress field. However, we treated domain NA in a different way. The solutions yielded nearly 80% thrusts (Figure 5). A small portion of mechanisms represents scattered extensional events, normal or oblique to the general shortening direction. Those mechanisms had to be separated from the compressional data set because of their kinematic incompatibility. We moved them into an extra data set NA-Ex. Furthermore, NA comprises an area of 300-km E-W extent. We split the set of compressional data into two subdomains NA-TW and NA-TE, west and east of the indenter corner. This should allow testing if a significant rotation of the orientation of σ_H exists. The subdomain boundary is indicated on the map in Figure 4.

In the following description, we use the terms transpression and transtension (Harland, 1971) for a combination of strike-slip and normal or reverse faulting (e.g., Dewey et al., 1998; Sanderson & Marchini, 1984). In Figure 6, we show the most important numeric results and diagrams of the SI calculation. We classified the stress regime based on the orientation of the principal axes, the distribution of PT axes, and the stress ratio. Domains GFS and EAE show a high scattering of PT-axes. These results need to be interpreted with caution. Domains with poor clustering of the principal stress axes can also be recognized in the confidence plots in Figure 6d and in a less pronounced maximum in the histogram in Figure 6e. The test for kinematic

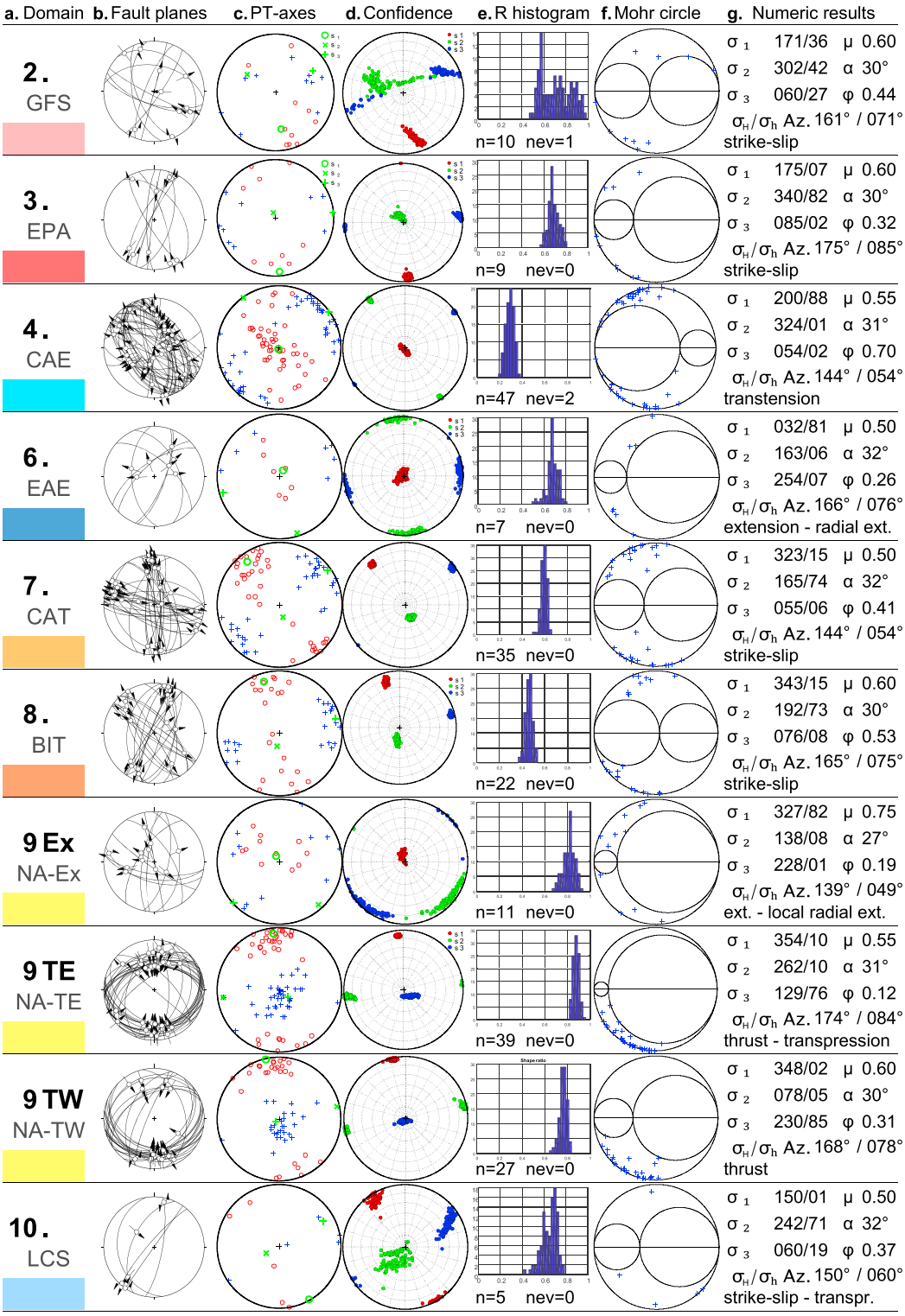

Figure 6. Results of the stress calculation with the SI method of Vavryčuk (2014), a derivative of the method of Michael (1984). (a) Domain no. and short name. (b) Angelier diagram of the faults selected from the pair of nodal planes by the method (lower hemisphere plot with fault plane as great circle and lineation including slip direction of hangingwall side). (c) Lower hemisphere plots of *P* (red circles) and *T* axes (blue crosses), drawn for $\alpha = 45°$. (d) Scatter plot showing the confidence limits of the principal stress directions for 100 noisy calculations. (e) Histogram of the shape ratio R for 100 noisy calculations. (f) Normalized Mohr circle, planes in upper/lower half: first/second nodal plane. (g) Numeric results: n/nev: total number of data sets/of data sets, which show an opposite slip sense than predicted from the calculated stress tensor; σ_{1-3}: orientation of principal stress axes; μ: friction coefficient selected for maximum overall fault instability; α: angle between slip vector and maximum principal stress; φ: stress ratio; σ_H, σ_h: azimuth of maximum/minimum horizontal stress.

compatibility of the mechanisms with respect to the bulk stress tensor was positive for all domains, except for GFS and CAE with one and two incompatible events, respectively.

The SI calculation optimized the friction coefficient μ between 0.50 and 0.75. Hence, the angle α calculated after equation (1) was close to 30°. This is a value commonly cited for newly formed shear fractures (e.g., Paterson & Wong, 2010; Zang & Stephansson, 2010). As shown in Figure 6, the principal stress axes for most domains are nearly horizontal and vertical. The method to distinguish the fault plane from the auxiliary plane searches for the highest instability following the Mohr-Coulomb criterion. Therefore, for the given stress orientation with nearly vertical and horizontal principal axes, thrusts close to 30° dip, normal faults close to 60° dip and strike-slip faults with strike around 30° from σ_1 were selected as more likely to be active (*Andersonian faults*; Anderson, 1951). We show these fault planes for orientation on the focal mechanism map (Figure 4) with thick black circles. However, a close look on the map reveals that in some cases, the computation chose fault planes, which do not fit to the regional fault pattern. This is most obvious for the PGF, where nodal planes perpendicular to the mapped fault were selected. We expect that reactivated faults could be active under unfavorable orientations with respect to the principal stress axes and that the mechanism searching for a maximum fault instability could fail in such cases. Further studies like relative relocations of the hypocenter distribution for main and aftershocks may better and independently constrain the selection of the correct nodal plane.

The transformation of the principal stress axes to σ_H and σ_h produced small azimuthal differences, with a maximum of 11° for domain GFS. Table S2 lists the azimuths of σ_H (λ_H for the NDA calculation) and the stress/strain ratio φ for the three different methods applied. For half of the domains the difference between the azimuths coming from GF and SI methods is at or below 10°. We observed rather large deviations of more than 20° for domains NA-Ex, NA-TE, and LCS. Generally, the azimuths calculated with SI and NDA methods do not diverge as much from each other as from the GF method. In many cases, results obtained with the GF method show a counterclockwise deviation compared to the results of the other two methods.

The NDA method (for results, see Figure S8) yielded a rather stable strain ratio, while the GF and SI methods tend to deviate stronger from $\varphi = 0.5$ for noncoaxial deformation components in a data set. This is obvious for thrust domain NA-TE with good data coverage and a clear thrust prevalence, where the NDA method yielded $\varphi = 0.43$ as would be expected for pure thrusting. SI and GF methods deviate into opposite directions, toward transpression (0.12; SI) and axial compression (0.75; GF), respectively. The GF algorithm calculates an average angular rotational misfit parameter, listed in Table S2. The misfits obtained, with a maximum of 6.1°, are below the angular precision of the focal mechanisms, which we estimate around 10° for most events.

Figure 7 illustrates the results of the stress calculations on the map. For an arbitrary point within each domain or subdomain, the arrows indicating the stress regime show the azimuths of σ_H and σ_h (λ_H and λ_h). We found similar orientations of the principal stress/strain axes in all domains, with one axis subhorizontal NW to NNW directed, one subhorizontal NE to ENE directed and the third axis subvertical. Generally, we observed a small clockwise rotation of the subhorizontal axes from west to east. The principal axes can swap their position in this frame, so that all stress regimes, such as thrusting, strike-slip, and normal faulting, are evident.

6.3.2. The Indenter Boundaries

(GFS) The mechanisms show a broad scatter of PT axes (Figure 6c). The spread is caused by the alignment of the nodal planes, one oriented parallel to the indenter boundary, which bends at the northern corner. Additionally, an extensional event (2.04) superimposes the strike-slip events. The slip sense of event 2.10 is opposite than predicted from the calculated stress tensor (nev in Figure 6e). In combination with the small number of mechanisms (10), the NNW directed σ_H direction must be regarded as an estimate.

(EPA) For the eastern Periadriatic realm, we calculated a strike-slip tensor with NNW directed σ_H (Figure 6g). For all events, the SI algorithm selected the north striking plane from the nodal pair, which is at right angle to the PGF (cf. Figure 4). The stress ratio and PT axis distribution indicate a trend to transpression. The data cluster well in Figure 6d. However, because of the small amount of input data (9), the result is not very well constrained. The principal stress axes west (GFS) and east of the indenter corner (EPA) diverge about 10–15°.

6.3.3. Extension and Strike-Slip Faulting West, North, and East of the Indenter Corner

(CAE) All three calculation methods gave transtensional φ values (Table S2), which fit the dominant normal faulting, mixed with strike-slip mechanisms. The extensional direction σ_h points to NE. The transtensional

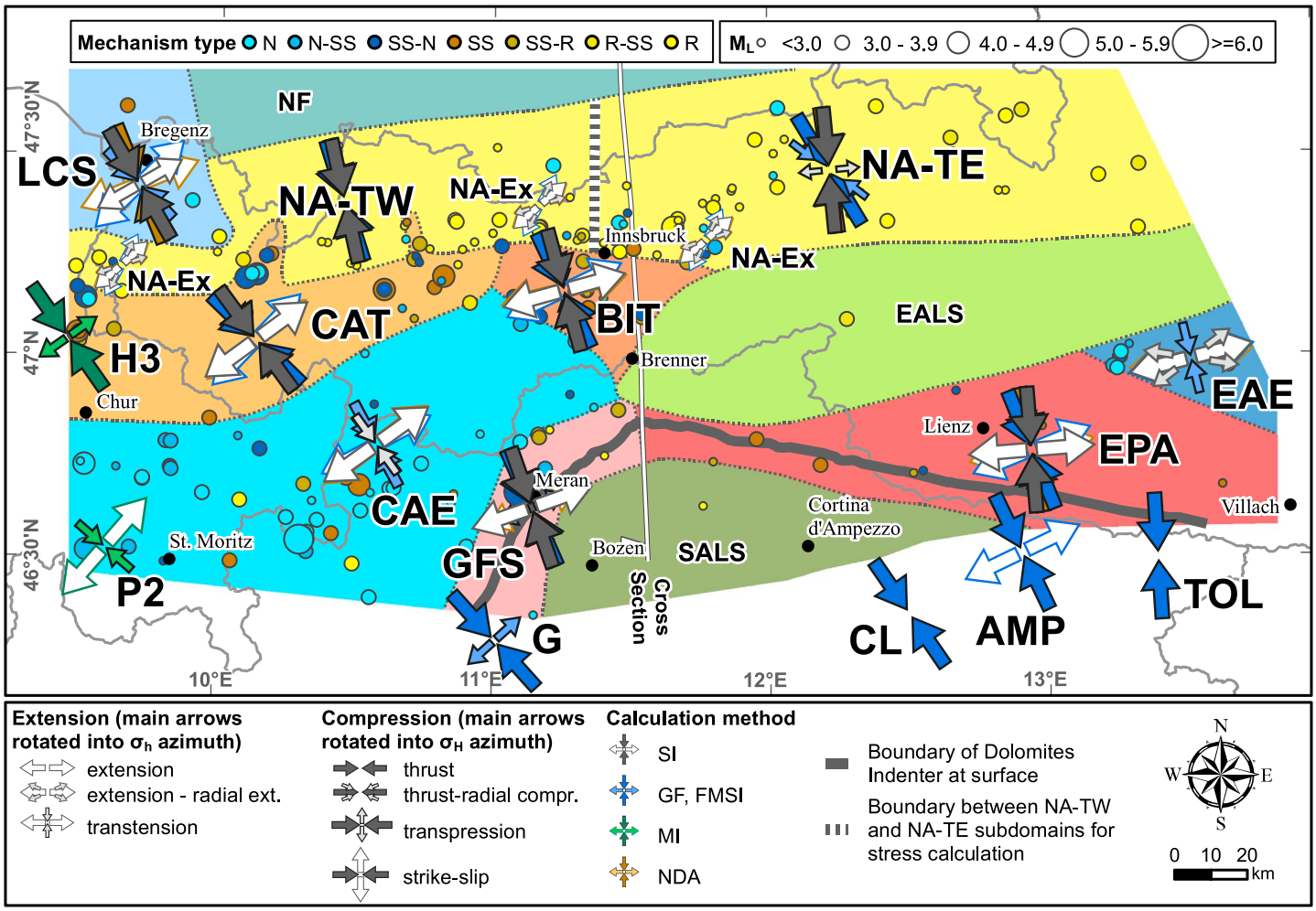

Figure 7. Map showing the results of the stress calculation in the seismotectonic domains/subdomains defined by the results of the focal mechanism calculations. For comparison we show also neighboring data sets H3 (Marschall et al., 2013), P2 (Kastrup et al., 2004), G (Viganò et al., 2008), and CL, AMP, TOL (Bressan et al., 2003). The central part of the orogen is characterized by strike-slip domains GFS, EPA, CAT, and BIT, and by the transtensional domain CAE west of and the extensional domain EAE at the SE margin of the Tauern Window. We observed a thrust regime south of the northern margin of the Alpine chain (NA-TW and NA-TE), with local extension (NA-Ex) and minor strike-slip influence (NA-TE). Upper crustal thrust mechanisms are superimposed by strike-slip faulting at mid to lower crustal level in the northwestern corner of the area of investigation (LCS). Calculation methods cited are SI (Vavryčuk, 2014), GF (Gephart & Forsyth, 1984), FMSI (Gephart, 1990), MI (Michael, 1984), and NDA (Spang, 1972). Numerical input is available in supporting Data Set S9.

character of the data set can be recognized from the well-established belt of *P* axes through the center of Figure 6c. Two data sets (4.01, 4.26) failed in the kinematic test (nev).

(EAE) At the southeastern boundary of our working area, we obtained mechanisms for seven events, showing two slightly different oriented extensional directions. The stress ratio $\varphi < 0.5$ indicates an affinity to radial extension. Due to the small amount of data and the scattering of PT axes, the ENE directed σ_H direction must be regarded as a rough estimate.

6.3.4. Transitional Domains Between the Indenter and the Northern Alps

Domain CAT is characterized by a strike-slip tensor, with stress ratios around 0.5 and NW directed σ_H. The stress calculation produced slightly counterclockwise rotated σ_H axes compared to the neighboring domains CAE and BIT.

Domain BIT shows a strike-slip to transtensional stress tensor with clockwise rotation of the stress axes as compared to domain CAT. The stress ratio is closer to 0.5 than in domain CAE, that is, the stress regime changes from transtension toward strike slip. This is also visible in the PT axis distribution in Figure 6c, where the *P* axes cluster at the diagram margins in BIT and are aligned along a belt in domain CAE.

6.3.5. The Northern Sector of the Eastern Alps

Data Set NA-T (all events from domain NA, except extensional mechanisms) yielded a thrust tensor. We observed a minimal but not significant divergence in thrust directions between the western (NA-TW) and eastern part (NA-TE) of this domain. Subset NA-TE (blue events in domain NA in Figure 7) shows a less pronounced clustering of the steeply aligned *T* axes (Figure 6c). This affects the φ value of the SI and GF methods, which deviate into different directions from 0.5, whereas the NDA method indicates pure thrusting. West of 12°E longitude, we detected distributed mechanisms indicating NE to ENE directed extensional stress conditions (subset NA-Ex). We show these extensional stress directions in three positions within NA on the map of Figure 7. This should indicate that we locally observed NE directed extension. However, due to the small number of mechanisms and the wide geographical spread, those results are not significant with respect to a general extensional direction and probably indicate local stress field variations.

Our data set comprises five events in domain LCS, with different mechanism types (strike-slip, thrust, and extension). Therefore, only a general NW directed shortening direction could be inferred. One extensional event (10.02) is located in the upper crust and might indicate local orogen-parallel extension, comparable to neighboring data set NA-Ex to the east.

7. Discussion

7.1. Orogen-Scale Transect Through the Corner of the Dolomites Indenter

We use a cross section from the northern Alpine foreland to the central DI to discuss our results (Figure 8). We simplified a profile by Brandner (2013), based on Brandner et al. (2008), and extended to the north and to depth following Ortner et al. (2006). Their section runs along the TRANSALP seismic line, located 30 km east of the profile presented here (cf. Figure 1). Structures were projected horizontally toward west. We indicate tectonic boundaries at great depth that are not visible in geophysical data as *speculative* in Figure 8. The most important features of the transect with respect to our study are as follows (numbers refer to details labeled in Figure 8):

1. The top of Europe is well constrained in the TRANSALP seismic section. Ortner et al. (2006) interpreted basement-involved thrusting within the European plate, shown in our section in a depth of 10 to 20 km, some kilometer north and south below the Inn valley at surface.
2. About 25 km south of the Inn Valley, the seismic section shows south dipping reflections that can be traced further south below the TW. The TRANSALP Working Group et al. (2002) related these reflections to the *Sub-Tauern ramp*. Below the Inn Valley, the thrust in continuation of this ramp branches (Figure 8). The most important splay is the IF, reaching the surface in a subvertical orientation (Ortner et al., 2006). For further discussion, we call these kinematically linked faults *Sub-Tauern thrust system*.
3. The steep northward dip of the PGF is drawn based on surface and tunnel data (Brandner et al., 2008). The DI is characterized by structures crossing the entire crust, which were interpreted as *Sub-Dolomites ramp* (TRANSALP Working Group et al., 2002). Here we draw two north dipping faults. Following Castellarin, Nicolich, et al. (2006), we connect the upper fault with the Valsugana thrust system (4) and the deeper one with the South Alpine frontal thrust (5).

For both plates, the position of the Moho is shown after Kummerow et al. (2004), based on receiver function data. Between the geophysically imaged European (6) and (7) Adriatic Mohos, there is a region where this boundary could not be resolved. (8) We left the tectonic interpretation for this zone and the relationship between the Sub-Tauern ramp and the Sub-Dolomites ramps open.

We projected earthquake hypocenters perpendicularly into the section within a maximum distance of 12 km, except event 2.02, which was brought into the section along strike of the nearby GF. We discuss the seismicity in detail in section 7.3.

7.2. Surface Kinematics

In this chapter, we discuss geodetic measurements to compare them to our results. South of the Alps, permanent-GNSS time series (Global Navigation Satellite Systems) indicate a N-NE directed movement of stations located in northeast Italy, relative to a stable European reference frame (region A in Figure 9b). Horizontal station velocities indicate ~1–2 mm/a shortening across the south Alpine thrust front in the Friuli area. Velocities decrease westward along the thrust. This movement is commonly attributed to the

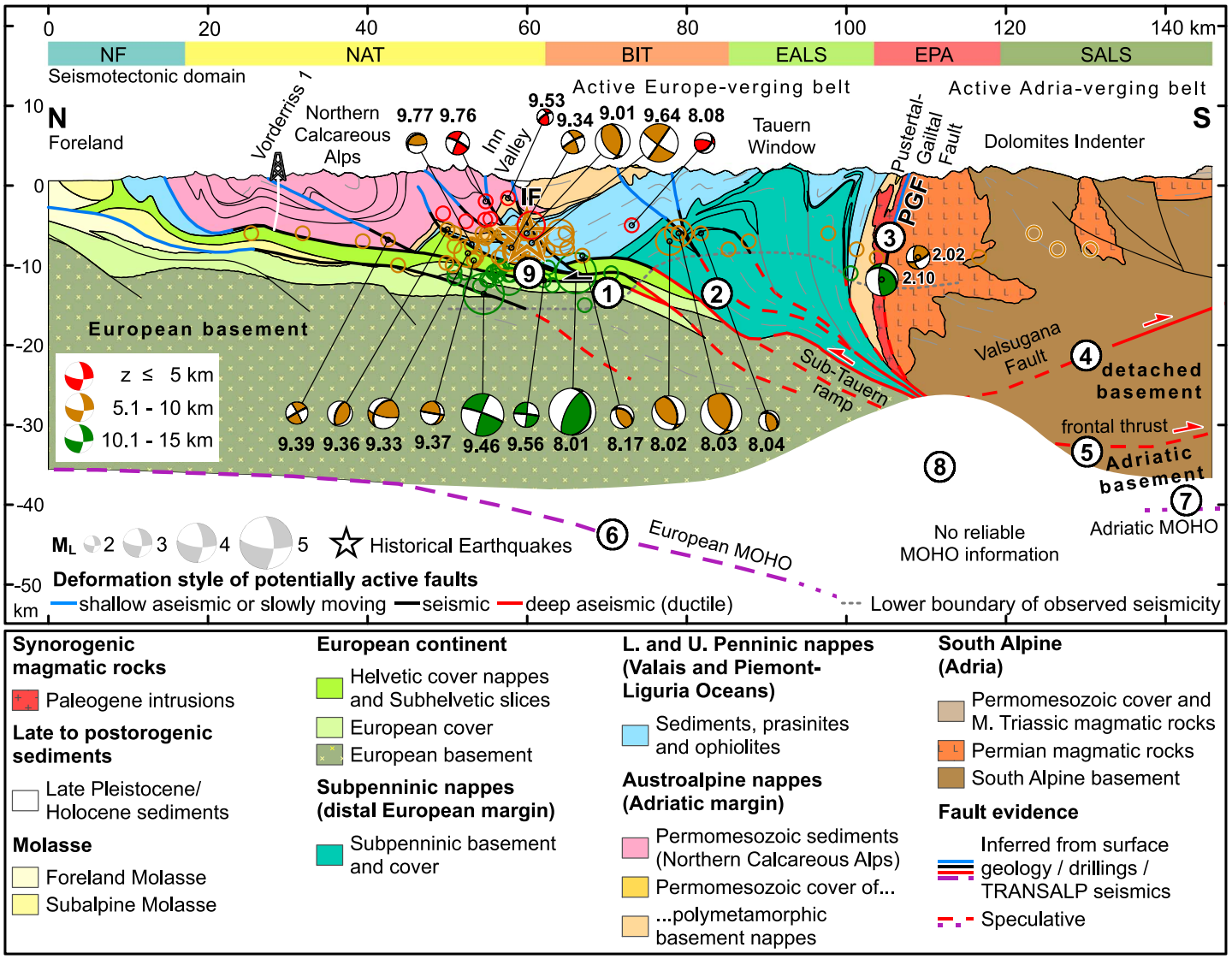

Figure 8. N-S cross section through the central Eastern Alps, extended, simplified and depth-extrapolated from Brandner et al. (2008), using the interpretation of the TRANSALP seismic line by Ortner et al. (2006). The profile trace is shown on the preceding maps. Surface geology from Bayerisches Landesamt für Umwelt (2015) in Bavaria, Geologische Bundesanstalt (2017a, 2017b) in northern Austria and Brandner (1980a) for the Italian sector south of the PGF. Subsurface geology of the Vorderriss 1 drill hole from Bachmann and Müller (1981). For the extension to depth and to north and south, we used TRANSALP deep seismic reflection data (Lüschen et al., 2004) and a line drawing of the TRANSALP Working Group et al. (2002). The Moho position is drawn from the velocity model of Kummerow et al. (2004). The profile trace is shown on the preceding maps. On top of the section, we indicate the seismotectonic domains defined in chapter 6.2 and shown on the maps of Figures 4, 7, and 9a. Focal mechanisms are shown in lower hemisphere diagrams, rotated into the section. Numbers next to them correspond to the map in Figures 4 and S1 and Table S1.

counterclockwise rotation of the Adria microplate (e.g., Métois et al., 2015; Sánchez et al., 2018, and references therein). No major changes in GNSS velocities are visible in the northern and western sector of the DI (Figure 9b). The movement direction is similar to Adria, but the north directed component is considerably smaller. Between regions A and DI, a transition zone with decreasing north directed velocities can be observed (vertical hatch in Figure 9b). Since no big earthquake has occurred during the period of GNSS observations, Cheloni et al. (2014) assume interseismic coupling and infer a locked South Alpine thrust front.

GNSS directions and velocities near the Eastern/Central Alps transition (CA in Figure 9b) are similar to stable Europe. Between regions DI and CA, a very small sinistral movement can be inferred, as shown in the shear

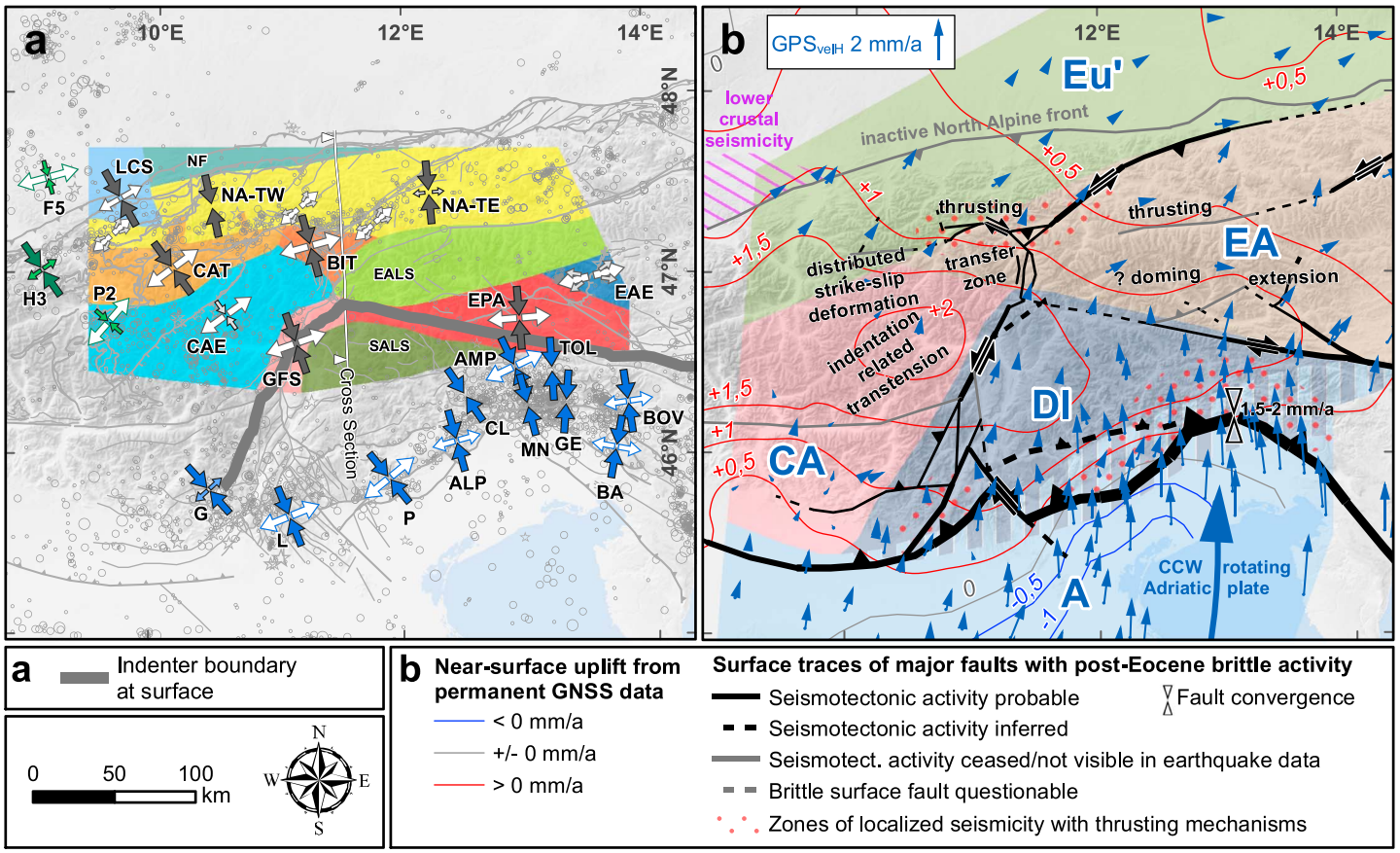

Figure 9. Overview maps to illustrate stress and strain around the Dolomites indenter. (a) Seismicity, faults, seismotectonic domains, and stress field. For a legend of the seismotectonic domains and stress symbols, see Figure 8. Stress regime and directions from this study, except H3, P2: Marschall et al. (2013); F5: Kastrup et al. (2004); G: Viganò et al. (2008); L, P, ALP: Restivo et al. (2016); CL, AMP, MN, TOL, GE, BOV, and BA: Bressan et al. (2003). (b) Simplified tectonic sketch showing seismotectonically active and ceased faults, horizontal Global Navigation Satellite Systems (GNSS) velocities relative to a Eurasia-fixed reference frame from (Métois et al., 2015) and isolines of a GNSS-inferred vertical deformation model with respect to IGb08 reference frame from (Sánchez et al., 2018). The areal extent of the transfer zone Alps-Jura (detached Molasse) was inferred after Malz et al. (2016). Digital elevation model from European Environment Agency (2013). For tectonic interpretation of the GNSS velocities, we colored different regions A, DI, CA, EA, and Eu', see text for details.

strain model of Sánchez et al. (2018). The northward velocity in the central part of the Eastern Alps (EA in Figure 9b) is comparable to region DI. However, the eastward velocity is significantly higher. At the eastern margin of our working area, the strain model of Sánchez et al. (2018) shows an onset of dextral shear between the Eastern Alps and the indenter, as can also be inferred by the clockwise rotation of arrows north of the PGF in Figure 9b.

With regard to the Eurasian reference frame of Métois et al. (2015), the northern foreland and the northwestern margin of the Eastern Alps (region Eu' in Figure 9b) move toward NE/ENE. Compared to region EA, the north component is slightly lower, but there is no visible difference in the east directed velocity (Métois et al., 2015). This is also supported by a recent GNSS velocity solution of Austrian stations by Madzak et al. (2017) and the data set of Sánchez et al. (2018). East of our working area, the data of Madzak et al. (2017) show an increase of the east directed velocity component of stations in the Eastern Alps, compared to regions EA and Eu'. According to the GNSS deformation rates and strain models (Métois et al., 2015; Sánchez et al., 2018), surface movement rates on single faults in our research area must be well below 1 mm/a.

Figure 9b shows isolines of a near-surface vertical movement model derived from GNSS data, calculated by Sánchez et al. (2018). Their results indicate a zone of maximum uplift of approximately 2 mm/a around 10°E/46.5°N. A zone of high uplift extends from there toward the east. The GNSS results are in line with repeated precise leveling campaigns of Austria (Ruess & Mitterschiffthaler, 2015) and Switzerland

(Brockmann et al., 2012), which reveal more details but do not cover the entire research area and jump across network boundaries. The strongest uplift gradient can be observed close to the South Alpine thrust front, with isolines parallel to thrust strike. This suggests a connection between thrusting and uplift/subsidence (Sánchez et al., 2018). For the remaining study area, the vertical velocity pattern does not correlate with extension or thrusting derived from our earthquake investigations. Apart from active faulting, uplift may be a superposition of isostasy related to the Alpine crustal root and postglacial isostatic rebound (e.g., Mey et al., 2016). Due to the low expected fault slip rates, we infer that only a minor portion of vertical surface movements is caused by active faulting, at the resolution of the model not being visible in the GNSS data.

7.3. Active Seismogenic Faulting

7.3.1. The DI and Its Boundaries

We relate the low seismicity in the northern part of the DI (domain SALS) to a high crustal strength above the north dipping detachments that link to the thrust fronts close to the southern indenter boundary (4 and 5 in Figure 8). This assumption is in line with a high effective elastic thickness inferred for the indenter from thermo-rheologic data (Stewart & Watts, 1997; Willingshofer & Cloetingh, 2003). Willingshofer and Cloetingh (2003) projected seismic events from a 50-km-wide zone into the TRANSALP section. Slightly different to our results, they show more hypocenters within the indenter, which also extend down to 35 km. This reflects an increase of the seismicity within the indenter towards east, as visible in Figure 2. Single events extending deeper than 15 km are visible in Figure 2 but are outside of the corridor of our section in Figure 8.

West/southwest of the indenter corner (domain CAE), we observed transtension. Strike-slip focal mechanisms from this area have one nodal plane parallel to the GFS. Extension occurs at an acute angle to the indenter boundary. A similar effect was shown in analogue models with two indenters moving at different velocities. In the transfer zone between the indenters—in our case the area west of the GF—K. Reiter et al. (2011) describe extension along the strike of this zone. Toward the north, extension mostly disappears and strike-slip deformation prevails in domain CAT. This may be related to a decrease and the end of the influence of indentation.

The strike of nodal planes in domains GFS and EPA follows the corner of the indenter boundary. We expect the section of the GFS located in our study area to be active because epicenters are located close to the surface trace of mapped faults and one nodal plane is commonly oriented parallel to it (e.g., Forst-Fault; Caporali et al., 2005; Viganò et al., 2015). Several events west of the Passeier Valley (2.06., 2.07, and 2.08) show focal mechanisms comparable to the Meran earthquake on the Forst Fault (2.03) and are aligned along strike. For the GF segment NE of Meran (cf. Figure 1), we obtained two fault plane solutions (2.02 and 2.10) of which one plane is parallel to the major fault strike. In cross section (Figure 8), event 2.10 could be located on the north dipping GF. Despite the low seismicity, events 3.01, 3.02, 3.08, and 3.09 suggest a seismically active PGF. The remarkable rotation of the azimuth of the horizontal GNSS velocities across the PGF as shown in Figure 9b may indicate creeping behavior of the fault. Activity of the MF is not supported by seismicity and focal mechanisms, except event 3.03. Low seismicity in domain EPA can be explained by small deviatoric stresses in the seismogenic zone, not large enough to generate new brittle faults. However, major faults as the PGF are in a favorable orientation to be reactivated in the present-day stress field.

7.3.2. The Tauern Window and Its Surroundings

The western and central TW (domain EALS) is almost aseismic. Major anisotropies within the seismogenic zone such as tectonic and lithologic boundaries are steeply inclined to subvertical and parallel to the general window strike and thus in an unfavorable orientation for reactivation in the present-day stress field (Figures 1 and 8). Additionally, a lack of elevated pore pressures could be the reason that such faults do not slip (cf. Faulkner et al., 2006). As in domain EPA, we infer that deviatoric stresses are not large enough to cause rupture of new brittle faults in the seismogenic zone. The lower boundary of the hypocenter distribution rises when approaching domain EALS from north and south (dashed line in Figure 8). We infer that the brittle-ductile transition follows this trend. This could be an effect of quartz-rich rocks, a low deformation rate, a higher temperature gradient, or any combination out of these. According to Chen et al. (2013), the lower boundary of the seismogenic zone would roughly coincide with a temperature of 350 ± 50 °C. The result is in line with a thermal model along the TRANSALP deep seismic section by Willingshofer and Cloetingh (2003), showing a rise of isotherms and the inferred brittle-ductile transition below the TW. However, Speranza et al. (2016) did not find such a temperature rise within the TW in their study on Curie point depth, based on spectral analysis of aeromagnetic residuals. Shallow Curie temperature depths in their map roughly

fit the area of maximum uplift shown in Figure 9b. Remarkable is the sector of minimum total lithospheric strength in the model of Willingshofer and Cloetingh (2003), which is located roughly below our EALS domain. According to their model, this minimum is not related to a smaller strength of the nappe pile but to a low contribution of the European lower crust and lithospheric mantle below the Sub-Tauern ramp to the total strength.

At the southeastern margin of the TW, we observed brittle extension parallel and oblique to orogen strike. In contrast to the Brenner area, where seismogenic normal faulting occurs in the hanging wall of the BF, extension in domain EAE is located in both the footwall and hangingwall of the KF. As our data suggest, this extension is very localized. Bertrand et al. (2017) suggested normal faulting activity of the KF at least until the Pliocene, based on AFT ages of up to 3 Ma in the footwall. Events 6.01 and 6.02 support ongoing activity of this fault (Figure 4). Extension in domain EAE could be an indication of active lateral extrusion in the sense of Ratschbacher, Frisch, et al. (1991). North of the PGF and west of the KF, the data sets of Métois et al. (2015), Madzak et al. (2017), and Sánchez et al. (2018) do not indicate an increase of the east component of the GNSS velocities from west to east (cf. Figure 9b and section 7.2). Therefore, the GNSS data do not support the lateral extrusion model in this part of our working area. Alternatively, like in domain CAE, extension at the SE margin of the TW could possibly be caused by the influence of a *subindenter*, limited by the MF, ZWD, and PGF (cf. Figure 1; Favaro et al., 2017; Kurz & Neubauer, 1996).

North of the indenter corner, domain BIT that encloses the BF, separates two areas of contrasting deformation style: strike-slip faulting with N-S shortening and minor E-W extension west of the BF and a lack of significant seismotectonic deformation east of it (*transfer zone* in Figure 9b). The orientation of strike-slip faults is comparable to the area CAE west of the indenter. The strike of normal faults is rotated clockwise with respect to CAE. The results indicate that extension, which dominates domain CAE, reaches to the BF (e.g., events 8.05 and 8.08). At the northern termination of the BF, steeply SW dipping, and vertical NW trending normal and strike-slip faults were mapped to the west of the main fault trace (Figure 1). Several events (8.06, 8.12, 8.15, 8.17, and 8.22) are located close to these faults and show strike-slip mechanisms, one plane being parallel to mapped fault. Therefore we presume, that the mapped extensional and strike-slip faults are still active. The extension observed north of the indenter corner is probably responsible for an increase in east directed GNSS velocities from region CA to region EA (Figure 9b). This setting can partially be compared to Miocene kinematics as described by Ratschbacher, Frisch, et al. (1991) and Rosenberg et al. (2018).

East of domain BIT, we could not retrieve any strike-slip focal mechanisms, which would indicate a seismotectonic activity of the western continuation of the SEMP fault (cf. Figures 1 and 4). West of the meridian of Salzburg, there is no evidence of seismicity related to the SEMP fault system (Figure 2), which is in line with the results from GNSS studies (chapter 7.2).

7.3.3. The Northern Part of the Eastern Alps

About 50 km north of the indenter corner, we observed a remarkable concentration of seismicity. This zone extends approximately 10 km north and south of the Inn Valley and approximately 50 km west and east of the northern BF termination (Figures 2 and 9b). Many hypocenters are located near the plate boundary (detail 9 in Figure 8). Seismic events likely extend down to the depth of inferred inversion structures as imaged in the TRANSALP section (Ortner et al., 2006; F. Reiter et al., 2003). Partially, the hypocenters plot in the inferred thrust splay in the Alpine nappe stack below and north of the Inn Valley. Shallow events ($z < 5$ km) cluster north of the valley (Figure 8). In many cases, moderately south dipping nodal planes are parallel to the basal detachment or thrusts in the inferred splay (Figure 8). Some of the thrusts in the nappe stack might be blind, terminating in folds. The broad scattering of events in map view (Figure 2) and section (Figure 8) can be attributed to an areal spread on moderately dipping thrusts.

We interpret this zone of thrusting as the northern and upward continuation of the Sub-Tauern ramp. It trends E-W, parallel to the inferred strike of the basal thrust. On the map, the IF crosses the area of thrusts diagonally (Figure 2). We infer that present-day thrusting now overprints older strike-slip faulting in the western part of the IF, where the fault bends toward a more restraining strike (cf. Figure 1). Thrust directions in domain NA point to N-NNW, perpendicular to fold axes in the Subalpine Molasse (Ortner et al., 2015). There is no significant change of their orientation west or east of the indenter corner. This is in contrast to the shortening direction in all other domains nearer to the indenter boundary where we found a clockwise rotation from west to east (Figures 7 and 9a).

Fault plane solutions from the close vicinity of the IF surface trace contain only one strike-slip focal mechanism with a nodal plane parallel to the main fault (9.01; Table S1). South of the Inn Valley, in the footwall of the BF, we observed strike-slip faulting mechanisms with one of the nodal planes striking parallel or oblique to the IF (8.01–8.04, 8.09, and 8.17, cf. Figure 8). Our results suggest, that steeply dipping minor faults between the TW and the Inn Valley are oriented unfavorable for thrusting and accommodate sinistral strike-slip movement (Figures 4 and 8). GNSS results across the zone of localized seismicity—despite the low station density in this area—do not indicate a significant velocity contrast (Figure 9b). Since no major earthquake has occurred during the GNSS period, we infer a low deformation rate and locked major faults.

About 20 km north of the Inn Valley, seismicity disappears; thus, no focal mechanisms could be determined. Probably, only a minor part of N-S convergence is transferred to this area, where the major thrust contacts successively approach the surface (Figure 8). The absence of seismicity is in line with a lack of differential GNSS movements (cf. section 7.2).

7.4. Stress Field

In this section, we compare our stress calculations to neighboring areas. Viganò et al. (2008) computed stress tensors for the Giudicarie (*G*) and Lessini (L) regions. The result of their domain G fits well with our calculations for domain GFS and is shown in Figures 7 and 9a. The direction of maximum horizontal stress rotates slightly clockwise when moving from domain G toward the northern indenter corner. Earthquake-derived stress calculations from the southeastern indenter area by Bressan et al. (2003) yielded similar results as in our domain EPA. Their domains CL, AMP, and TOL are shown on the stress maps in Figures 7 and 9a.

The results from our domain CAE are in accordance with data set P2 from Switzerland (Marschall et al., 2013). Compared to domain P2, we observed a clockwise rotation of σ_h. The stress tensor of domain CAT fits well to domain H3 of Marschall et al. (2013) further west (Figures 7 and 9a). The orientation of principal stress axes in domain F5 of Kastrup et al. (2004) and our domain LCS is similar. However, due to the low number of data sets, our results should be regarded as preliminary.

The stress data derived from focal mechanisms in domains CAE and BIT are partially in line with in situ stress measurements from deep drill holes and cores east of the BF (Braun & Reinhold, 2017). These data show N to NNW directed maximum principal stresses north and south of the Brenner Pass and extension with ESE directed minimum stress in a drill hole at the central western end of the TW.

Between the transtensional/extensional domains CAE and EAE, we found a transition zone (BIT) with a strike-slip to transtensional tensor (Figure 7). Northwest of these central zones, a strike-slip stress field, which continues to the Swiss part of the central Alps, ends north of the indenter tip (CAT). The northernmost part of the central Eastern Alps is thrust dominated (NA-T), without significant influence of the DI on the greater regional stress field. Stress directions become parallel to the more uniform first order directions (Zoback, 1992), as shown on the world stress map (Heidbach et al., 2016).

7.5. Comparison to Models and Experiments for Neogene Indentation

North-directed, seismogenic thrusting is concentrated in a zone approximately 30 km north of the indenter tip (Figure 9b). This thrusting probably started during the Late Miocene, after the end of foreland propagation of the Alpine wedge (Ortner et al., 2015). Strength profiles of the Alpine lithosphere commonly comprise a high strength of the lithospheric mantle, which contributes most to the total lithospheric strength (e.g., van Gelder et al., 2017; Willingshofer & Cloetingh, 2003). We suggest that active stacking in domain NA is caused by north directed push of the lithospheric mantle from the undetached part of Adria (*deep indentation*). We explain this push by convergence at the South Alpine thrust front, which is proven by GNSS data. Following the interpretation of the TRANSALP section with trans-crustal ramps (Figure 8), Adria push could be transferred to the deeper part of the Alpine nappe pile and into the European crust, utilizing the Sub-Tauern thrust system in front of the indenter. Our data suggest basement-involved thrusting, currently propagating toward the foreland and inverting previously undeformed parts of the upper European plate. The Sub-Tauern thrust system and Sub-Dolomites ramps are probably both active, the units of the hanging wall forming a double wedge. On the Adria side, a southward propagating thrust sequence is obvious. It started with Valsugana thrusting (Middle-Late Miocene) and migrated to the Montello front with the Messinian (Castellarin, Vai, et al., 2006).

Within the Alpine nappe stack, we observed a disturbance of the stress and strain field, caused by the detached, upper portion of the indenter (*shallow indentation*). Deformation and stress are partially comparable to indentation and lateral extrusion models. In their physical analogue models, Ratschbacher et al. (1991) moved a triangular indenter northward. Indentation experiments of Rosenberg et al. (2004) and Rosenberg et al. (2007) revealed that NNE directed indentation generated structures with the greatest similarities compared to surface geology. However, published GNSS data, in line with our focal mechanism and stress results (Figure 9), indicate that present-day indentation is NNW directed.

Extension west of the indenter boundary as discussed in section 7.2. can be interpreted as a lateral effect of indentation, as shown in the model of K. Reiter et al. (2011). Since this extensional zone extends further westward (Kastrup et al., 2004; Marschall et al., 2013), we infer a continuous transition to their domain *P2* with extension oblique to orogen strike, which they relate to uplift, topography and density variations.

Rosenberg et al. (2004) describe a westward increase of orogen-parallel extension at the surface of their model that reaches a maximum north of the indenter tip. The GNSS movement pattern (Figure 9b) and our results are different. East of the indenter tip, in domain EALS, we did not observe active extension in the seismogenic zone. Extensional focal mechanisms indicate that active, orogen parallel, and oblique extension starts 150 km east of the indenter tip, near the southeastern termination of the TW. GNSS data do not indicate an increase of the eastward crustal velocity between the BF and the eastern margin of our working area (Figure 9b), but further east (cf. section 7.2). Additionally, in our working area, no gradient of the east-directed velocity component can be observed between units in the central Eastern Alpine area and the northern foreland (Métois et al., 2015). If an ongoing lateral extrusion process exists here, it might either be extremely slow or involve the northern foreland.

In the area of localized seismicity with thrusting mechanisms, we would expect N-S shortening (cf. Figure 9b). However, GNSS results (section 7.2), show only a minimal decrease of the northward velocity component across this area. This might be explained by a very low surface velocity and a lack of creep, which means that interseismic deformation (no earthquake with significant displacement occurred during the GNSS period) is distributed across a wide area.

Additionally, minor strike-slip movements at NE striking faults between the TW and the Inn Valley should partially accommodate the north directed component and cause an increase of the east component to the south. This cannot be observed in the GNSS velocities (Figure 9b). Either this contradicts with the classical extrusion model of Ratschbacher, Merle, et al. (1991) or differential movements might be hidden in the GNSS data due to very low surface velocities.

8. Conclusions

1. The DI governs seismotectonic deformation in terms of focal mechanism type and deflects the orientation of the regional stress field around its northern corner. The western indenter boundary (GFS) is characterized by active sinistral faulting. The northeastern boundary (PGF) moves dextrally with minor seismicity and, according to GNSS data, with a very low rate.
2. The regions bordering the indenter to the west and north are characterized by transtension, influenced by indentation. In an approximately 70-km-wide zone away from the indenter boundary, the minimum horizontal stress rotates clockwise from west to east by 10–20°. Farther away, the deviation from the overall stress field is not as pronounced. No deflection of the greater regional stress field could be observed north of the Inn Valley.
3. The broad zone of seismicity to the north and south of the Inn Valley, 50 km west and east of Innsbruck, is related to the Sub-Tauern thrust system. The basal Alpine detachment and reverse faults within the upper part of the European plate are active. An almost total lack of earthquakes north of this zone suggests that N-S shortening is accommodated here in blind thrusts and thrusts reaching the surface in the southern part of the NCA. Probably, the major faults, connecting to the surface, are locked, governing a smooth deformation pattern as shown by the GNSS data.
4. The detached part of the DI, the TW, and the Austroalpine south of the seismically active zone of (3) together form a double wedge. The units are separated from the underlying, deeper parts, by two active thrust systems: the Sub-Tauern thrust system in the north and the Sub-Dolomites ramps in the south. Small deviatoric stresses within this double wedge might be responsible for minor internal deformation and activity on preexisting faults (e.g., PGF and IF system).

5. The western end of the Inntal fault today compensates convergence from thrusting of the Sub-Tauern ramp. Based on focal mechanisms, a system of faults, consisting of the IF and parallel subordinate sinistral strike-slip faults between the IF and the TW, still accommodates minor eastward movement of the western TW.
6. The undetached part of Adria, bounded by the Sub-Dolomites ramps and the GFS, pushes into the region of the descending plate boundary between Europe and the Alpine nappe pile. This deep indentation causes thrusting mentioned above in (4) and successively detaches slices from the European basement.
7. We did not find evidence for significant active, seismogenic faulting within the western TW. Possible reasons are small deviatoric stresses and an orientation of weakness zones subperpendicular to the principal stress axes.
8. The configuration at the western margin of extrusion has changed: eastward movement of central eastern Alpine crust is visible in GNSS data, with regard to the DI and the units west of the BF. The southern boundary of extruding crust at the PGF can be recognized in earthquake and GNSS data. The northern boundary of the extrusion corridor may be located at the IF but is not evident for the western SEMP. More rapid, east directed movement of Alpine crust in the central parts of the orogen might begin east of the TW.
9. Vertical crustal movements caused by thrusting or normal faulting are very small and can hardly be recognized in the velocity pattern of GNSS stations. Isostatic effects are probably significantly greater than vertical movements generated from active faulting.

Statement

There are no real or perceived financial conflicts of interests for any of the authors.

Acknowledgments
We are grateful to T. Kraft for supporting us with data from his thesis. We thank J. Wassermann for help with the Bavarian seismological network, V. Vavryčuk for help on the SI software, and V. Blaž and R. Barsch for support with ObsPy. A. Snoke kindly answered questions about FocMec. From ZAMG we thank R. Meurers, Y. Jia, and N. Horn for support. E. Priolo provided help regarding the OASIS data center; V. Lauciani and S. Mazza helped with INGV data access. Many thanks to E. Kissling for enabling access to the AlpArray network and to G. Bokelmann for supporting that. We appreciate the work of the AlpArray working group very much. Information about member institutions and names of persons is available at http://www.alparray.ethz.ch. We are grateful to H. Pomella and A. Viganò for discussions about their research. We thank A. Caporali, G. Stangl, M. Madzak, and P. Mitterschiffthaler for discussions about GNSS data. Thanks to E. Brückl and M. Behm for information about their velocity model. We thank the following seismological services for providing data: Bundesanstalt für Geowissenschaften und Rohstoffe, Bayrischer Erdbebendienst, Geoforschungszentrum Potsdam, Istituto Nazionale di Geofisica e Vulcanologia, Istituto Nazionale di Oceanografia e di Geofisica Sperimentale, Schweizerischer Erdbebendienst, and National Earthquake Services of Slovenia, Croatia and the Czech Republic. As part of the data set of Diehl et al. (2009), we used waveforms from the Swiss NAGRA, the networks of Baden-Württemberg and Rheinland-Pfalz, and the University of Cologne. We are grateful to M. Rauch, Autonome Provinz Bozen, for permitting access to the SI network. F. R. was partially funded by the Federal Government of Tyrol and the Austrian Government (research project BMBWK-VIII/A/5-14027408), the Brenner Base Tunnel SE, and the Public Employment Service Austria (AMS). The authors thank Claudio Rosenberg, one anonymous reviewer, and the Associate Editor Ernst Willingshofer for their constructive and helpful comments. Supporting information includes eight figures, two tables, and eight supporting data sets. Waveform data used from network OE are available at https://doi.org/10.6084/m9.figshare.5596726 Access to AlpArray data is restricted. See http://www.alparray.ethz.ch/en/seismic_network/backbone/data-access/ for data access.

References

Agostinelli, G., Comin, C., Mair, V., Pedemonte, S., & Velicogna, A. (1995). The "Fleres" tunnel: Some geological-technical data. *Gallerie e grandi Opere Sotterranee*, *46*(7), 45–53.
Aki, K., & Richards, P. G. (2002). *Quantitative seismology* (2nd ed.). Sausalito, CA: University Science Books.
AlpArray Working Group (2015). AlpArray Seismic Network (AASN) temporary component. https://doi.org/10.12686/alparray/z3_2015
Álvarez-Gómez, J. A. (2014). FMC: A one-liner Python program to manage, classify and plot focal mechanisms. Paper presented at EGU General Assembly 2014, Vienna.
Anderson, E. M. (1951). *The dynamics of faulting and dyke formation with applications to Britain* (2nd ed.). Edinburgh: Oliver and Boyd.
Angelier, J. (1979). Determination of the mean principal directions of stresses for a given fault population. *Tectonophysics*, *56*(3-4), T17–T26. https://doi.org/10.1016/0040-1951(79)90081-7
Angelier, J. (2002). Inversion of earthquake focal mechanisms to obtain the seismotectonic stress IV—A new method free of choice among nodal planes. *Geophysical Journal International*, *150*(3), 588–609. https://doi.org/10.1046/j.1365-246X.2002.01713.x
Autonome Provinz Bozen (2017). CARGBrowser: geologische Übersicht. Retrieved from http://gis2.provinz.bz.it/carg/ClientServlet?CMD=Init
Bachmann, G. H., & Müller, M. (1981). Geologie der Tiefbohrung Vorderriß 1 (Kalkalpen, Bayern). *Geologica Bavarica*, *81*, 17–53.
Baer, M., Deichmann, N., Ballarin Dolfin, D., Bay, F., Delouis, B., Fäh, D., et al. (1999). Earthquakes in Switzerland and surrounding regions during 1998. *Eclogae Geologicae Helvetiae*, *92*(2), 265–273. https://doi.org/10.5169/seals-168668
Baer, M., Deichmann, N., Braunmiller, J., Ballarin Dolfin, D., Bay, F., Bernardi, F., et al. (2001). Earthquakes in Switzerland and surrounding regions during 2000. *Eclogae Geologicae Helvetiae*, *94*(2), 253–264. https://doi.org/10.5169/seals-168893
Baer, M., Deichmann, N., Braunmiller, J., Clinton, J., Husen, S., Fäh, D., et al. (2007). Earthquakes in Switzerland and surrounding regions during 2006. *Swiss Journal of Geosciences*, *100*(3), 517–528. https://doi.org/10.1007/s00015-007-1242-0
Baer, M., Deichmann, N., Braunmiller, J., Husen, S., Fäh, D., Giardini, D., et al. (2005). Earthquakes in Switzerland and surrounding regions during 2004. *Eclogae Geologicae Helvetiae*, *98*(3), 407–418. https://doi.org/10.1007/s00015-005-1168-3
Bartel, E. M., Neubauer, F., Genser, J., & Heberer, B. (2014). States of paleostress north and south of the Periadriatic fault: Comparison of the Drau Range and the Friuli Southalpine wedge. *Tectonophysics*, *637*(Supplement C), 305–327. https://doi.org/10.1016/j.tecto.2014.10.019
Basili, R., Valensise, G., Vannoli, P., Burrato, P., Fracassi, U., Mariano, S., et al. (2008). The Database of Individual Seismogenic Sources (DISS), version 3: Summarizing 20 years of research on Italy's earthquake geology. *Tectonophysics*, *453*(1-4), 20–43. https://doi.org/10.1016/j.tecto.2007.04.014
Bayerisches Landesamt für Umwelt (2015). Geologische Karte von Bayern 1:500.000-WMS. Retrieved from http://www.lfu.bayern.de/gdi/wms/geologie/gk500?
Behm, M. (2009). 3-D modelling of the crustal *S*-wave velocity structure from active source data: application to the Eastern Alps and the Bohemian Massif. *Geophysical Journal International*, *179*(1), 265–278. https://doi.org/10.1111/j.1365-246X.2009.04259.x
Behm, M., Brückl, E., Chwatal, W., & Thybo, H. (2007). Application of stacking and inversion techniques to three-dimensional wide-angle reflection and refraction seismic data of the Eastern Alps. *Geophysical Journal International*, *170*(1), 275–298. https://doi.org/10.1111/j.1365-246X.2007.03393.x
Behrmann, J. H. (1988). Crustal-scale extension in a convergent orogen: the Sterzing-Steinach mylonite zone in the Eastern Alps. *Geodinamica Acta*, *2*(2), 63–73. https://doi.org/10.1080/09853111.1988.11105157
Benedetti, L., Tapponnier, P., King, G. C. P., Meyer, B., & Manighetti, I. (2000). Growth folding and active thrusting in the Montello region, Veneto, northern Italy. *Journal of Geophysical Research*, *105*(B1), 739–766. https://doi.org/10.1029/1999JB900222

Bernardi, F., Braunmiller, J., & Giardini, D. (2005). Seismic moment from regional surface-wave amplitudes: Applications to digital and analog seismograms. *Bulletin of the Seismological Society of America*, *95*(2), 408–418. https://doi.org/10.1785/0120040048

Bertrand, A., Rosenberg, C., & Garcia, S. (2015). Fault slip analysis and late exhumation of the Tauern Window, Eastern Alps. *Tectonophysics*, *649*, 1–17. https://doi.org/10.1016/j.tecto.2015.01.002

Bertrand, A., Rosenberg, C., Rabaute, A., Herman, F., & Fügenschuh, B. (2017). Exhumation mechanisms of the Tauern Window (Eastern Alps) inferred from apatite and zircon fission track thermochronology. *Tectonics*, *36*, 207–228. https://doi.org/10.1002/2016TC004133

Beyreuther, M., Barsch, R., Krischer, L., Megies, T., Behr, Y., & Wassermann, J. (2010). ObsPy: A python toolbox for seismology. *Seismological Research Letters*, *81*(3), 530–533. https://doi.org/10.1785/gssrl.81.3.530

Bigi, G., Castellarin, A., Coli, M., Dal Piaz, G. V., & Vai, G. B. (1990). Structural model of Italy. Sheet N.2, (scale 1:500.000). Rome: Consiglio Nazionale Delle Ricerce.

Blanckenburg, F. v., Kagami, H., Deutsch, A., Oberli, F., Meier, M., Wiedenbeck, M., et al. (1998). The origin of Alpine plutons along the Periadriatic Lineament. *Schweizerische Mineralogische und Petrographische Mitteilungen*, *78*(1), 55–66. https://doi.org/10.5169/seals-59274

Blanckenburg, F. v., Villa, I. M., Baur, H., Morteani, G., & Steiger, R. H. (1989). Time calibration of a PT-path from the Western Tauern Window, Eastern Alps: The problem of closure temperatures. *Contributions to Mineralogy and Petrology*, *101*(1), 1–11. https://doi.org/10.1007/BF00387196

Bondár, I., Myers, S. C., Engdahl, E. R., & Bergman, E. A. (2004). Epicentre accuracy based on seismic network criteria. *Geophysical Journal International*, *156*(3), 483–496. https://doi.org/10.1111/j.1365-246X.2004.02070.x

Bott, M. H. P. (1959). The mechanics of oblique slip faulting. *Geological Magazine*, *96*(2), 109–117. https://doi.org/10.1017/S0016756800059987

Bousquet, R., Schmid, S. M., Zeilinger, G., Oberhänsli, R., Rosenberg, C., & Molli, G. (2012). Tectonic framework of the Alps, (scale 1:1.000.000). Commission for the Geological Map of the World. Retrieved from http://www.geodynalps.org

Brandner, R. (1980a). Geologische Übersichtskarte von Tirol, (scale 1:300.000). Innsbruck: Universitätsverlag Wagner.

Brandner, R. (1980b). Tektonische Übersichtskarte von Tirol, (scale 1:600.000). Innsbruck: Universitätsverlag Wagner.

Brandner, R. (2013). *Alpenprofil. Institute for Geology*. Innsbruck: University of Innsbruck. https://doi.org/10.13140/RG.2.2.20466.81603

Brandner, R., Reiter, F., & Töchterle, A. (2008). Überblick zu den Ergebnissen der geologischen Vorerkundung für den Brenner-Basistunnel. *Geo.Alp*, *5*, 165–174.

Braun, R., & Reinhold, C. (2017). Ermittlung von 3D Gebirgsspannungszuständen für den Brenner Basistunnel. *Geotechnik*, 1–15. https://doi.org/10.1002/gete.201600025

Braunmiller, J., Kradolfer, U., Baer, M., & Giardini, D. (2002). Regional moment tensor determination in the European–Mediterranean area—Initial results. *Tectonophysics*, *356*(1–3), 5–22. https://doi.org/10.1016/S0040-1951(02)00374-8

Bressan, G., Bragato, P. L., & Venturini, C. (2003). Stress and strain tensors based on focal mechanisms in the seismotectonic framework of the Friuli–Venezia Giulia Region (Northeastern Italy). *Bulletin of the Seismological Society of America*, *93*(3), 1280–1297. https://doi.org/10.1785/0120020058

Brockmann, E., Ineichen, D., Marti, U., Schaer, S., Schlatter, A., & Villiger, A. (2012). Determination of tectonic movements in the Swiss Alps using GNSS and levelling. Paper presented at the Geodesy for Planet Earth, Berlin, Heidelberg. https://doi.org/10.1007/978-3-642-20338-1_85

Bundesamt für Landestopografie (2005). Tektonische Karte der Schweiz (GK500-Tekto), (scale 1:500.000). Wabern.

Burrato, P., Eliana Poli, M., Vannoli, P., Zanferrari, A., Basili, R., & Galadini, F. (2008). Sources of M_w 5+ earthquakes in northeastern Italy and western Slovenia: An updated view based on geological and seismological evidence. *Tectonophysics*, *453*(1-4), 157–176. https://doi.org/10.1016/j.tecto.2007.07.009

Butterworth, S. (1930). On the theory of filter amplifiers. *Experimental Wireless and the Wireless Engineer*, *7*, 536–541.

Byerly, P. (1955). Nature of faulting as deduced from seismograms. In A. Poldervaart (Ed.), *Crust of the Earth: A symposium* (pp. 75–86). GSA Special Papers, Geological Society of America.

Caporali, A., Braitenberg, C., & Massironi, M. (2005). Geodetic and hydrological aspects of the Merano earthquake of 17 July 2001. *Journal of Geodynamics*, *39*(4), 317–336. https://doi.org/10.1016/j.jog.2005.01.001

Caputo, R., Poli, M. E., & Zanferrari, A. (2010). Neogene–Quaternary tectonic stratigraphy of the eastern Southern Alps, NE Italy. *Journal of Structural Geology*, *32*(7), 1009–1027. https://doi.org/10.1016/j.jsg.2010.06.004

Castellarin, A., & Cantelli, L. (2000). Neo-Alpine evolution of the Southern Eastern Alps. *Journal of Geodynamics*, *30*(1-2), 251. https://doi.org/10.1016/S0264-3707(99)00036-8

Castellarin, A., Fesce, A. M., Picotti, V., Pini, G. A., Prosser, G., Sartori, R., et al. (1987). Structural and kinematic analysis of the Giudicarie deformation belt. Implications for compressional tectonics of Southern Alps. *Mineralogica et Petrographica Acta*, *30*, 287–310.

Castellarin, A., Nicolich, R., Fantoni, R., Cantelli, L., Sella, M., & Selli, L. (2006). Structure of the lithosphere beneath the Eastern Alps (southern sector of the TRANSALP transect). *Tectonophysics*, *414*(1), 259–282. https://doi.org/10.1016/j.tecto.2005.10.013

Castellarin, A., Vai, G. B., & Cantelli, L. (2006). The Alpine evolution of the Southern Alps around the Giudicarie Faults: A Late Cretaceous to Early Eocene transfer zone. *Tectonophysics*, *414*(1), 203–233. https://doi.org/10.1016/j.tecto.2005.10.019

Célérier, B. (1995). Tectonic regime and slip orientation of reactivated faults. *Geophysical Journal International*, *121*(1), 143–161. https://doi.org/10.1111/j.1365-246X.1995.tb03517.x

Célérier, B., Etchecopar, A., Bergerat, F., Vergely, P., Arthaud, F., & Laurent, P. (2012). Inferring stress from faulting: From early concepts to inverse methods. *Tectonophysics*, *581*(Supplement C), 206–219. https://doi.org/10.1016/j.tecto.2012.02.009

Cheloni, D., D'Agostino, N., & Selvaggi, G. (2014). Interseismic coupling, seismic potential, and earthquake recurrence on the southern front of the Eastern Alps (NE Italy). *Journal of Geophysical Research: Solid Earth*, *119*, 4448–4468. https://doi.org/10.1002/2014JB010954

Chen, W.-P., Yu, C.-Q., Tseng, T.-L., Yang, Z., Wang, C.-y., Ning, J., & Leonard, T. (2013). Moho, seismogenesis, and rheology of the lithosphere. *Tectonophysics*, *609*, 491–503. https://doi.org/10.1016/j.tecto.2012.12.019

Crotwell, P. H., & Owens, T. J. (2016). The TaupP Toolkit: Flexible seismic travel-time and raypath utilities (Version 2.4). South Carolina: University of South Carolina, Department of Geological. *Sciences*. Retrieved from http://www.seis.sc.edu/downloads/TauP/taup.pdf

Decker, K., Peresson, H., & Faupl, P. (1994). Die miozäne Tektonik der östlichen Kalkalpen: Kinematik, Paläospannungen und Deformationsaufteilung während der "lateralen Extrusion" der Zentralalpen. *Jahrbuch der Geologischen Bundesanstalt*, *137*, 5–18.

Decker, K., & Reiter, F. (2003). Die duktil-spröde Deformation am Westrand des Tauernfensters. Paper presented at Arbeitstagung der Geologischen Bundesanstalt, Trins.

Deichmann, N. (1992). Structural and rheological implications of lower-crustal earthquakes below northern Switzerland. *Physics of the Earth and Planetary Interiors*, *69*, 270–280. https://doi.org/10.1016/0031-9201(92)90146-M

Deichmann, N., Baer, M., Braunmiller, J., Ballarin Dolfin, D., Bay, F., Bernardi, F., et al. (2002). Earthquakes in Switzerland and surrounding regions during 2001. *Eclogae Geologicae Helvetiae*, *96*(2), 313–324. https://doi.org/10.5169/seals-168958

Deichmann, N., Baer, M., Braunmiller, J., Husen, S., Fäh, D., Giardini, D., et al. (2006). Earthquakes in Switzerland and surrounding regions during 2005. *Eclogae Geologicae Helvetiae*, *99*(3), 443–452. https://doi.org/10.5169/seals-169249
Deichmann, N., Clinton, J., Husen, S., Edwards, B., Haslinger, F., Fäh, D., et al. (2010). Earthquakes in Switzerland and surrounding regions during 2009. *Swiss Journal of Geosciences*, *103*(3), 535–549. https://doi.org/10.1007/s00015-010-0039-8
Deichmann, N., Clinton, J., Husen, S., Edwards, B., Haslinger, F., Fäh, D., et al. (2011). Earthquakes in Switzerland and surrounding regions during 2010. *Swiss Journal of Geosciences*, *104*(3), 537–547. https://doi.org/10.1007/s00015-011-0084-y
Deichmann, N., Clinton, J., Husen, S., Edwards, B., Haslinger, F., Fäh, D., et al. (2012). Earthquakes in Switzerland and surrounding regions during 2011. *Swiss Journal of Geosciences*, *105*(3), 463–476. https://doi.org/10.1007/s00015-012-0116-2
Dewey, J. F., Holdsworth, R. E., & Strachan, R. A. (1998). Transpression and transtension zones. *Geological Society, London, Special Publications*, *135*(1), 1–14. https://doi.org/10.1144/gsl.sp.1998.135.01.01
Dewey, J. F., Pitman, W. C. III, Ryan, W. B. F., & Bonnin, J. (1973). Plate tectonics and the evolution of the alpine system. *Geological Society of America Bulletin*, *84*(10), 3137–3180. https://doi.org/10.1130/0016-7606(1973)84<3137:PTATEO>2.0.CO;2
Diehl, T., Clinton, J., Kraft, T., Husen, S., Plenkers, K., Guilhelm, A., et al. (2014). Earthquakes in Switzerland and surrounding regions during 2013. *Swiss Journal of Geosciences*, *107*(2-3), 359–375. https://doi.org/10.1007/s00015-014-0171-y
Diehl, T., Deichmann, N., Clinton, J., Husen, S., Kraft, T., Plenkers, K., et al. (2013). Earthquakes in Switzerland and surrounding regions during 2012. *Swiss Journal of Geosciences*, *106*(3), 543–558. https://doi.org/10.1007/s00015-013-0154-4
Diehl, T., Husen, S., Kissling, E., & Deichmann, N. (2009). High-resolution 3-D *P*-wave model of the Alpine crust. *Geophysical Journal International*, *179*(2), 1133–1147. https://doi.org/10.1111/j.1365-246X.2009.04331.x
Eisbacher, G., & Brandner, R. (1995). Role of high-angle faults during heteroaxial contraction, Inntal thrust sheet, Northern Calcareous Alps, Western Austria. *Geologisch-Paläontologische Mitteilungen der Universität Innsbruck*, *20*, 389–406.
European Environment Agency (2013, Last update: 2015-06-25). Digital Elevation Model over Europe (EU-DEM). Retrieved from https://www.eea.europa.eu/data-and-maps/data/eu-dem
Evans, R. (1984). Effects of the free surface on shear wavetrains. *Geophysical Journal International*, *76*(1), 165–172. https://doi.org/10.1111/j.1365-246X.1984.tb05032.x
Faulkner, D. R., Mitchell, T. M., Healy, D., & Heap, M. J. (2006). Slip on 'weak' faults by the rotation of regional stress in the fracture damage zone. *Nature*, *444*, 922. https://doi.org/10.1038/nature05353
Favaro, S., Handy, M. R., Scharf, A., & Schuster, R. (2017). Changing patterns of exhumation and denudation in front of an advancing crustal indenter, Tauern Window (Eastern Alps). *Tectonics*, *36*, 1053–1071. https://doi.org/10.1002/2016TC004448
Finetti, I., Russi, M., & Slejko, D. (1979). The Friuli earthquake (1976–1977). *Tectonophysics*, *53*(3), 261–272. https://doi.org/10.1016/0040-1951(79)90070-2
Förtsch, O., & Schmedes, E. (1976). Untersuchungen der seismischen Aktivität im Nordteil der Geotraverse IA. *Geologische Rundschau*, *65*(2), 748–755. https://doi.org/10.1007/BF01808491
Frisch, W., Dunkl, I., & Kuhlemann, J. (2000). Post-collisional orogen-parallel large-scale extension in the Eastern Alps. *Tectonophysics*, *327*(3-4), 239–265. https://doi.org/10.1016/S0040-1951(00)00204-3
Frisch, W., Kuhlemann, J., Dunkl, I., & Brügel, A. (1998). Palinspastic reconstruction and topographic evolution of the Eastern Alps during late Tertiary tectonic extrusion. *Tectonophysics*, *297*(1-4), 1–15. https://doi.org/10.1016/S0040-1951(98)00160-7
Frohlich, C. (1996). Cliff's nodes concerning plotting nodal lines for *P*, S_h and S_v. *Seismological Research Letters*, *67*(1), 16–24. https://doi.org/10.1785/gssrl.67.1.16
Fügenschuh, B., Seward, D., & Mancktelow, N. S. (1997). Exhumation in a convergent orogen: the western Tauern window. *Terra Nova*, *9*(5-6), 213–217. https://doi.org/10.1111/j.1365-3121.1997.tb00015.x
Galadini, F., & Galli, P. (1999). Palaeoseismology related to the displaced Roman archaeological remains at Egna (Adige Valley, northern Italy). *Tectonophysics*, *308*(1-2), 171–191. https://doi.org/10.1016/S0040-1951(99)00080-3
Galadini, F., Poli, M. E., & Zanferrari, A. (2005). Seismogenic sources potentially responsible for earthquakes with $M \geq 6$ in the eastern Southern Alps (Thiene-Udine sector, NE Italy). *Geophysical Journal International*, *161*(3), 739–762. https://doi.org/10.1111/j.1365-246X.2005.02571.x
Ganas, A., Gosar, A., & Drakatos, G. (2008). Static stress changes due to the 1998 and 2004 Krn Mountain (Slovenia) earthquakes and implications for future seismicity. *Natural Hazards and Earth System Sciences*, *8*, 59–66. https://doi.org/10.5194/nhess-8-59-2008
Genser, J., & Neubauer, F. (1989). Low angle normal faults at the eastern margin of the Tauern window (Eastern Alps). *Mitteilungen der Österreichischen Geologischen Gesellschaft*, *81*, 233–243.
Geologische Bundesanstalt (2017a). GEOFAST, compiled geological maps of Austria [WMS service]. Vienna. Retrieved from https://gisgba.geologie.ac.at/arcgis/services/image/AT_GBA_GEOFAST/ImageServer/WMSServer?request=GetCapabilities
Geologische Bundesanstalt (2017b). Geological maps of Austria 1:50.000 [WMS service]. Vienna. Retrieved from https://gisgba.geologie.ac.at/arcgis/services/image/AT_GBA_GK50/ImageServer/WMSServer?request=GetCapabilities
Gephart, J. W. (1990). FMSI: A Fortran program for inverting fault/slickenside and earthquake focal mechanism data to obtain the regional stress tensor. *Computers & Geosciences*, *16*(7), 953–989. https://doi.org/10.1016/0098-3004(90)90105-3
Gephart, J. W., & Forsyth, D. W. (1984). An improved method for determining the regional stress tensor using focal mechanism data: Application to the San Fernando earthquake sequence. *Journal of Geophysical Research*, *89*(B11), 9305–9320. https://doi.org/10.1029/JB089iB11p09305
Groshong, R. H. Jr. (1974). Experimental test of least-squares strain gage calculation using twinned calcite. *GSA Bulletin*, *85*(12), 1855–1864. https://doi.org/10.1130/0016-7606(1974)85<1855:ETOLSG>2.0.CO;2
Hammerl, C. (2017). Historical earthquake research in Austria. *Geoscience Letters*, *4*(1), 7. https://doi.org/10.1186/s40562-017-0073-8
Handy, M. R., Schmid, S. M., Bousquet, R., Kissling, E., & Bernoulli, D. (2010). Reconciling plate-tectonic reconstructions of Alpine Tethys with the geological–geophysical record of spreading and subduction in the Alps. *Earth-Science Reviews*, *102*(3), 121–158. https://doi.org/10.1016/j.earscirev.2010.06.002
Harland, W. B. (1971). Tectonic transpression in Caledonian Spitsbergen. *Geological Magazine*, *108*(1), 27–41. https://doi.org/10.1017/S0016756800050937
Heberer, B., Reverman, R. L., Fellin, M. G., Neubauer, F., Dunkl, I., Zattin, M., et al. (2017). Postcollisional cooling history of the Eastern and Southern Alps and its linkage to Adria indentation. *International Journal of Earth Sciences*, *106*(5), 1557–1580. https://doi.org/10.1007/s00531-016-1367-3
Heidbach, O., Custodio, S., Kingdon, A., Mariucci, M. T., Montone, P., Müller, B., et al. (2016). Stress map of the Mediterranean and Central Europe 2016. https://doi.org/10.5880/WSM.2016.001
Hejl, E. (1997). 'Cold spots' during the Cenozoic evolution of the Eastern Alps: thermochronological interpretation of apatite fission-track data. *Tectonophysics*, *272*(2), 159–173. https://doi.org/10.1016/S0040-1951(96)00256-9

Husen, S., Kissling, E., Deichmann, N., Wiemer, S., Giardini, D., & Baer, M. (2003). Probabilistic earthquake location in complex three-dimensional velocity models: Application to Switzerland. *Journal of Geophysical Research*, *108*(B2), 2077. https://doi.org/10.1029/2002JB001778

International Seismological Centre (2017). Bulletin of the International Seismological Centre. Retrieved from http://www.isc.ac.uk/iscbulletin/

Istituto Nazionale di Geofisica e Vulcanologia (2017, Last update: 2017-09-23). Time domain moment tensor catalogue. Retrieved from http://info.terremoti.ingv.it/en/tdmt

Istituto Nazionale di Oceanografia e di Geofisica sperimentale (2013). The OGS Archive System of Instrumental Seismology (OASIS). Retrieved from http://oasis.crs.inogs.it/oasis

Johnston, A. C., Coppersmith, K. J., Kanter, L. R., & Cornell, C. A. (1994). *The earthquakes of stable continental regions. Volume 1: Assessment of large earthquake potential (TR-102261-V1)*. Palo Alto CA: Electrical Power Research Institute (EPRI). Retrieved from https://www.epri.com/#/pages/product/TR-102261-V1/

Kastrup, U., Zoback, M. L., Deichmann, N., Evans, K. F., Giardini, D., & Michael, A. J. (2004). Stress feld variations in the Swiss Alps and the northern Alpine foreland derived from inversion of fault plane solutions. *Journal of Geophysical Research*, *109*, B01402. https://doi.org/10.1029/2003JB002550

Kaverina, A. N., Lander, A. V., & Prozorov, A. G. (1996). Global creepex distribution and its relation to earthquake-source geometry and tectonic origin. *Geophysical Journal International*, *125*(1), 249–265. https://doi.org/10.1111/j.1365-246X.1996.tb06549.x

Kennett, B. L. N., Engdahl, E. R., & Buland, R. (1995). Constraints on seismic velocities in the Earth from traveltimes. *Geophysical Journal International*, *122*(1), 108–124. https://doi.org/10.1111/j.1365-246X.1995.tb03540.x

Kraft, T. (1999). Die Seismizität der nördlichen Ostalpen und die Herdmechanik ausgewählter Erdbeben. (Msc thesis), Ludwig-Maximilians-Universität, Munich. https://doi.org/10.13140/RG.2.2.10056.21768

Kummerow, J., Kind, R., Oncken, O., Giese, P., Ryberg, T., Wylegalla, K., & Scherbaum, F. (2004). A natural and controlled source seismic profile through the Eastern Alps: TRANSALP. *Earth and Planetary Science Letters*, *225*(1-2), 115–129. https://doi.org/10.1016/j.epsl.2004.05.040

Kurz, W., & Neubauer, F. (1996). Deformation partitioning during updoming of the Sonnblick area in the Tauern Window (Eastern Alps, Austria). *Journal of Structural Geology*, *18*(11), 1327–1337. 1339-1343. https://doi.org/10.1016/S0191-8141(96)00057-0

Läufer, A. L., Frisch, W., Steinitz, G., & Loeschke, J. (1997). Exhumed fault-bounded alpine blocks along the Periadriatic Lineament—The Eder Unit (Carnic Alps, Austria). *Geologische Rundschau*, *86*(3), 312–626. https://doi.org/10.1007/s005310050167

Lavenu, A., & Cembrano, J. (1999). Compressional- and transpressional-stress pattern for Pliocene and Quaternary brittle deformation in fore arc and intra-arc zones (Andes of Central and Southern Chile). *Journal of Structural Geology*, *21*(12), 1669–1691. https://doi.org/10.1016/S0191-8141(99)00111-X

Lee, W. H., & Lahr, J. C. (1975). HYPO71 (revised): A computer program for determining hypocenter, magnitude, and first motion pattern of local earthquakes. Open-File Report. Menlo Park CA: United States, Department of the Interior, Geological Survey.

Lenhardt, W. A., Freudenthaler, C., Lippitsch, R., & Fiegweil, E. (2007). Focal-depth distributions in the Austrian Eastern Alps based on macroseismic data. *Austrian Journal of Earth Sciences*, *100*, 66–79.

Linzer, H.-G., Decker, K., Peresson, H., Dell'Mour, R., & Frisch, W. (2002). Balancing lateral orogenic float of the Eastern Alps. *Tectonophysics*, *354*(3-4), 211–237. https://doi.org/10.1016/S0040-1951(02)00337-2

Lomax, A. J. (2016). SeisGram2K seismogram viewer (Version 7.0.0X10). Mouans-Sartoux. Retrieved from http://alomax.free.fr/seisgram/SeisGram2K.html

Lomax, A. J., Virieux, J., Volant, P., & Berge-Therry, C. (2000). Probabilistic earthquake location in 3D and layered models: Introduction of a Metropolis-Gibbs method and comparison with linear locations. In C. H. Thurber, & N. Rabinowitz (Eds.), *Advances in seismic event location*, *Modern Approaches in Geophysics*, (pp. 101–134). Dordrecht: Springer.

Lund, B., & Slunga, R. (1999). Stress tensor inversion using detailed microearthquake information and stability constraints: Application to Ölfus in southwest Iceland. *Journal of Geophysical Research*, *104*(B7), 14947–14964. https://doi.org/10.1029/1999JB900111

Lund, B., & Townend, J. (2007). Calculating horizontal stress orientations with full or partial knowledge of the tectonic stress tensor. *Geophysical Journal International*, *170*(3), 1328–1335. https://doi.org/10.1111/j.1365-246X.2007.03468.x

Lüschen, E., Borrini, D., Gebrande, H., Lammerer, B., Millahn, K., Neubauer, F., & Nicolich, R. (2006). TRANSALP—Deep crustal Vibroseis and explosive seismic profiling in the Eastern Alps. *Tectonophysics*, *414*(1), 9–38. https://doi.org/10.1016/j.tecto.2005.10.014

Lüschen, E., Lammerer, B., Gebrande, H., Millahn, K., & Nicolich, R. (2004). Orogenic structure of the Eastern Alps, Europe, from TRANSALP deep seismic reflection profiling. *Tectonophysics*, *388*(1-4), 85–102. https://doi.org/10.1016/j.tecto.2004.07.024

Luth, S., Willingshofer, E., ter Borgh, M., Sokoutis, D., van Otterloo, J., & Versteeg, A. (2013). Kinematic analysis and analogue modelling of the Passeier- and Jaufen faults: implications for crustal indentation in the Eastern Alps. *International Journal of Earth Sciences*, *102*(4), 1071–1090. https://doi.org/10.1007/s00531-012-0846-4

Madzak, M., Mitterschiffthaler, P., & Stangl, G. (2017). Station velocities from a permanent GNSS network in the Eastern Alps. Paper presented at EGU General Assembly, Vienna.

Malz, A., Madritsch, H., Meier, B., & Kley, J. (2016). An unusual triangle zone in the external northern Alpine foreland (Switzerland): Structural inheritance, kinematics and implications for the development of the adjacent Jura fold-and-thrust belt. *Tectonophysics*, *670*, 127–143. https://doi.org/10.1016/j.tecto.2015.12.025

Mancktelow, N. S., Stöckli, D. F., Grollimund, B., Müller, W., Fügenschuh, B., Viola, G., et al. (2001). The DAV and Periadriatic fault systems in the Eastern Alps south of the Tauern window. *International Journal of Earth Sciences*, *90*(3), 593–622. https://doi.org/10.1007/s005310000190

Marschall, I., Deichmann, N., & Marone, F. (2013). Earthquake focal mechanisms and stress orientations in the eastern Swiss Alps. *Swiss Journal of Geosciences*, *106*(1), 79–90. https://doi.org/10.1007/s00015-013-0129-5

Martin, S., Bigazzi, G., Zattin, M., Viola, G., & Balestrieri, M. L. (1998). Neogene kinematics of the Giudicarie fault (Central-Eastern Alps, Italy): New apatite fission-track data. *Terra Nova*, *10*(4), 217–221. https://doi.org/10.1046/j.1365-3121.1998.00119.x

Martínez-Garzón, P., Kwiatek, G., Ickrath, M., & Bohnhoff, M. (2014). MSATSI: A MATLAB package for stress inversion combining solid classic methodology: A new simplified user-handling, and a visualization tool. *Seismological Research Letters*, *85*(4), 896–904. https://doi.org/10.1785/0220130189

Massari, F. (1990). The foredeeps of the northern Adriatic margin: Evidence of diachroneity in deformation of the Southern Alps. *Rivista Italiana di Paleontologia e Stratigrafia*. https://doi.org/10.13130/2039-4942/9043

McKenzie, D. P. (1969). The relation between fault plane solutions for earthquakes and the directions of the principal stresses. *Bulletin of the Seismological Society of America*, *59*(2), 591–601.

Meschede, M. (1994). *Methoden der Strukturgeologie*. Stuttgart: Ferdinand Enke.

Métois, M., D'Agostino, N., Avallone, A., Chamot-Rooke, N., Rabaute, A., Duni, L., et al. (2015). Insights on continental collisional processes from GPS data: Dynamics of the peri-Adriatic belts. *Journal of Geophysical Research: Solid Earth*, *120*, https://doi.org/10.1002/2015JB012023, 8701–8719.

Mey, J., Scherler, D., Wickert, A. D., Egholm, D. L., Tesauro, M., Schildgen, T. F., & Strecker, M. R. (2016). Glacial isostatic uplift of the European Alps. *Nature Communications*, *7*(13382), 1–9. https://doi.org/10.1038/ncomms13382

Michael, A. J. (1984). Determination of stress from slip data: Faults and folds. *Journal of Geophysical Research*, *89*(B13), 11517–11526. https://doi.org/10.1029/JB089iB13p11517

Michael, A. J. (1987). Use of focal mechanisms to determine stress: A control study. *Journal of Geophysical Research*, *92*(B1), 357–368. https://doi.org/10.1029/JB092iB01p00357

Müller, W., Prosser, G., Mancktelow, N. S., Villa, I. M., Kelley, S. P., Viola, G., & Oberli, F. (2001). Geochronological constraints on the evolution of the Periadriatic Fault System (Alps). *International Journal of Earth Sciences*, *90*, 623–653. https://doi.org/10.1007/s005310000187

Nussbaum, C. (2000). Neogene tectonics and thermal maturity of sediments of the easternmost Southern Alps. (PhD Thesis), University of Neuchâtel, Neuchâtel.

Ortner, H., Aichholzer, S., Zerlauth, M., Pilser, R., & Fügenschuh, B. (2015). Geometry, amount, and sequence of thrusting in the Subalpine Molasse of western Austria and southern Germany, European Alps. *Tectonics*, *34*, 1–30. https://doi.org/10.1002/2014TC003550

Ortner, H., Reiter, F., & Acs, P. (2002). Easy handling of tectonic data: the programs TectonicVB for Mac and TectonicsFP for Windows. *Computers & Geosciences*, *28*(10), 1193–1200. https://doi.org/10.1016/S0098-3004(02)00038-9

Ortner, H., Reiter, F., & Brandner, R. (2006). Kinematics of the Inntal shear zone-sub-Tauern ramp fault system and the interpretation of the TRANSALP seismic section, Eastern Alps, Austria. *Tectonophysics*, *414*(1-4), 241–258. https://doi.org/10.1016/j.tecto.2005.10.017

Paterson, M. S., & Wong, T.-f. (2010). *Experimental rock deformation—The brittle field* (2nd ed.). Berlin: Springer.

Pleuger, J., Mancktelow, N., Zwingmann, H., & Manser, M. (2012). K–Ar dating of synkinematic clay gouges from Neoalpine faults of the Central, Western and Eastern Alps. *Tectonophysics*, *550-553*, 1–16. https://doi.org/10.1016/j.tecto.2012.05.001

Poli, M. E., Peruzza, L., Rebez, A., Renner, G., Slejko, D., & Zanferrari, A. (2002). New seismotectonic evidence from the analysis of the 1976–1977 and 1977–1999 seismicity in Friuli. *Bollettino di Geofisica Teorica ed Applicata*, *43*(1-2), 53–78.

Pomella, H., Flöss, D., Speckbacher, R., Tropper, P., & Fügenschuh, B. (2016). The western end of the Eoalpine High-Pressure Belt (Texel unit, South Tyrol/Italy). *Terra Nova*, *28*(1), 60–69. https://doi.org/10.1111/ter.12191

Pomella, H., Klotz, T., Reiter, F., & Stipp, M. (2018). The Dolomites Indenter Italian Southern Alps. Deformation from Neoalpine indentation until today. Paper presented at European Geosciences Union General Assembly 2018, Vienna.

Pomella, H., Klötzli, U., Scholger, R., Stipp, M., & Fügenschuh, B. (2011). The Northern Giudicarie and the Meran-Mauls fault (Alps, Northern Italy) in the light of new paleomagnetic and geochronological data from boudinaged Eo-/Oligocene tonalites. *International Journal of Earth Sciences*, *100*(8), 1827–1850. https://doi.org/10.1007/s00531-010-0612-4

Pomella, H., Stipp, M., & Fügenschuh, B. (2012). Thermochronological record of thrusting and strike-slip faulting along the Giudicarie fault system (Alps, Northern Italy). *Tectonophysics*, *579*(Supplement C), 118–130. https://doi.org/10.1016/j.tecto.2012.04.015

Pondrelli, S., Ekström, G., & Morelli, A. (2001). Seismotectonic re-evaluation of the 1976 Friuli, Italy, seismic sequence. *Journal of Seismology*, *5*(1), 73–83. https://doi.org/10.1023/a:1009822018837

Pondrelli, S., Morelli, A., & Ekström, G. (2004). European-Mediterranean regional centroid-moment tensor catalog: solutions for years 2001 and 2002. *Physics of the Earth and Planetary Interiors*, *145*(1–4), 127–147. https://doi.org/10.1016/j.pepi.2004.03.008

Pondrelli, S., Morelli, A., Ekström, G., Mazza, S., Boschi, E., & Dziewonski, A. M. (2002). European–Mediterranean regional centroid-moment tensors: 1997–2000. *Physics of the Earth and Planetary Interiors*, *130*(1–2), 71–101. https://doi.org/10.1016/S0031-9201(01)00312-0

Prager, C. (2003). Das Brenner-Mesozoikum nördlich des Pflerschtals. Paper presented at Arbeitstagung der Geologischen Bundesanstalt, Trins.

Rathore, J. S., & Becke, M. (1980). Magnetic fabric analyses in the Gail Valley (Carinthia, Austria) for the determination of the sense of movements along this region of the Periadriatic Line. *Tectonophysics*, *69*(3), 349–368. https://doi.org/10.1016/0040-1951(80)90216-4

Ratschbacher, L., Frisch, W., Linzer, H.-G., & Merle, O. (1991). Lateral extrusion in the Eastern Alps, Part 2: Structural analysis. *Tectonics*, *10*(2), 257–271. https://doi.org/10.1029/90TC02623

Ratschbacher, L., Frisch, W., Neubauer, F., Schmid, S. M., & Neugebauer, J. (1989). Extension in compressional orogenic belts: The Eastern Alps. *Geology*, *17*(5), 404–407. https://doi.org/10.1130/0091-7613(1989)017<0404:EICOBT>2.3.CO;2

Ratschbacher, L., Merle, O., Davy, P., & Cobbold, P. (1991). Lateral extrusion in the Eastern Alps: Part 1, Boundary conditions and Experiments scaled for gravity. *Tectonics*, *10*(2), 245–256. https://doi.org/10.1029/90TC02622

Reicherter, K., Fimmel, R., & Frisch, W. (1993). Sinistral strike-slip faults in the Central Tauern Window (Eastern Alps, Austria): A short note. *Jahrbuch der Geologischen Bundesanstalt*, *136*, 495–502.

Reinecker, J., & Lenhardt, W. A. (1999). Present-day stress field and deformation in eastern Austria. *Geologische Rundschau*, *88*(3), 532–550. https://doi.org/10.1007/s005310050283

Reiser, M. (2010). Hydrological characterisation of Lake Obernberg, Brenner pass area, Tyrol. *Austrian Journal of Earth Sciences*, *103*(1), 43–57.

Reiter, F., & Lenhardt, W. A. (2006). FPS2 for Windows: A computer program for calculation and visualisation of fault plane solutions. Paper presented at PANGEO Austria 2006, Innsbruck. https://doi.org/10.13140/RG.2.2.20901.40163

Reiter, F., & Lenhardt, W. A. (2017). FPS for Windows: A computer program for calculation and visualisation of fault plane solutions (Version 4.5). Innsbruck. https://doi.org/10.13140/RG.2.2.11673.93286

Reiter, F., Lenhardt, W. A., & Brandner, R. (2005). Indications for activity of the Brenner Normal Fault zone (Tyrol, Austria) from seismological and GPS data. *Austrian Journal of Earth Sciences*, *97*, 16–23.

Reiter, F., Ortner, H., & Brandner, R. (2003). Seismically active Inntal fault zone: inverted European rift structures control upper plate deformation. *Memorie di Scienze Geologiche*, *54*(Speciale), 233–234.

Reiter, F., Ortner, H., Lenhardt, W. A., & Brandner, R. (2007). Evidence for activity of the Inn Valley fault zone (Tyrol, Austria) from earthquake and GPS data. Paper presented at EGU annual conference, Vienna.

Reiter, K., Kukowski, N., & Ratschbacher, L. (2011). The interaction of two indenters in analogue experiments and implications for curved fold-and-thrust belts. *Earth and Planetary Science Letters*, *302*(1), 132–146. https://doi.org/10.1016/j.epsl.2010.12.002

Restivo, A., Bressan, G., & Sugan, M. (2016). Stress and strain patterns in the Venetian Prealps (north-eastern Italy) based on focal-mechanism solutions. *Bollettino di Geofisica Teorica ed Applicata*, *57*(1), 13–30. https://doi.org/10.4430/bgta0166

Ritz, J.-F., & Taboada, A. (1993). Revolution stress ellipsoids in brittle tectonics resulting from an uncritical use of inverse methods. *Bulletin de la Société Géologique de France*, *164*(4), 519–531.

Robl, J., Heberer, B., Prasicek, G., Neubauer, F., & Hergarten, S. (2017). The topography of a continental indenter: The interplay between crustal deformation, erosion, and base level changes in the eastern Southern Alps. *Journal of Geophysical Research: Earth Surface*, *122*, 310–334. https://doi.org/10.1002/2016JF003884

Rockenschaub, M., Brandner, R., Decker, K., Priewalder, H., & Reiter, F. (2003). Geologie und Tektonik westlich des Wipptals. Paper presented at Arbeitstagung der Geologischen Bundesanstalt, Trins.

Rosenberg, C. L., Brun, J.-P., Cagnard, F., & Gapais, D. (2007). Oblique indentation in the Eastern Alps: Insights from laboratory experiments. *Tectonics*, *26*, TC2003. https://doi.org/10.1029/2006TC001960

Rosenberg, C. L., Brun, J.-P., & Gapais, D. (2004). Indentation model of the Eastern Alps and the origin of the Tauern Window. *Geology*, *32*(11), 997–1000. https://doi.org/10.1130/G20793.1

Rosenberg, C. L., & Garcia, S. (2011). Estimating displacement along the Brenner Fault and orogen-parallel extension in the Eastern Alps. *International Journal of Earth Sciences*, *100*(5), 1129–1145. https://doi.org/10.1007/s00531-011-0645-3

Rosenberg, C. L., & Schneider, S. (2008). The western termination of the SEMP Fault (eastern Alps) and its bearing on the exhumation of the Tauern Window. In S. Siegesmund, B. Fügenschuh, & N. Froitzheim (Eds.), *Tectonic aspects of the Alpine-Dinaride-Carpathian System* (Vol. 298, pp. 197–218). London: The Geological Society of London.

Rosenberg, C. L., Schneider, S., Scharf, A., Bertrand, A., Hammerschmidt, K., Rabaute, A., & Brun, J.-P. (2018). Relating collisional kinematics to exhumation processes in the Eastern Alps. *Earth-Science Reviews*, *176*(Supplement C), 311–344. https://doi.org/10.1016/j.earscirev.2017.10.013

Roth, P., Pavoni, N., & Deichmann, N. (1992). Seismotectonics of the Eastern Swiss Alps and evidence for precipitation induced variations of seismic activity. *Tectonophysics*, *207*(1-2), 183–197. https://doi.org/10.1016/0040-1951(92)90477-N

Ruess, D., & Mitterschiffthaler, P. (2015). Rezente Höhenänderungen in Österreich abgeleitet aus geodätischen Wiederholungsmessungen. Paper presented at 18. Internationale Geodätische Woche, Obergurgl.

Saint Louis University Earthquake Center (2017. Last update: 2017-04-08). Moment Tensor Inversions for Europe. Retrieved from http://www.eas.slu.edu/eqc/eqc_mt/MECH.EU/

Sánchez, L., Völksen, C., Sokolov, A., Arenz, H., & Seitz, F. (2018). Present-day surface deformation of the Alpine Region inferred from geodetic techniques. *Earth System Science Data*, *10*, 1503–1526. https://doi.org/10.5194/essd-10-1503-2018

Sanderson, D. J., & Marchini, W. R. D. (1984). Transpression. *Journal of Structural Geology*, *6*(5), 449–458. https://doi.org/10.1016/0191-8141(84)90058-0

Scharf, A., Handy, M. R., Favaro, S., Schmid, S. M., & Bertrand, A. (2013). Modes of orogen-parallel stretching and extensional exhumation in response to microplate indentation and roll-back subduction (Tauern Window, Eastern Alps). *International Journal of Earth Sciences*, *102*(6), 1627–1654. https://doi.org/10.1007/s00531-013-0894-4

Schmid, S. M., Aebli, H., Heller, F., & Zingg, A. (1989). The role of the Periadriatic Line in the tectonic evolution of the Alps. In M. P. Coward, D. Dietrich, & R. G. Park (Eds.), *Alpine Tectonics*, *Geological Society Special Publication* (Vol. 45, pp. 153–171). London: Geological Society. https://doi.org/10.1144/gsl.sp.1989.045.01.08

Schmid, S. M., Scharf, A., Handy, M. R., & Rosenberg, C. L. (2013). The Tauern Window (Eastern Alps, Austria): A new tectonic map, with cross-sections and a tectonometamorphic synthesis. *Swiss Journal of Geosciences*, *106*(1), 1–32. https://doi.org/10.1007/s00015-013-0123-y

Schmid, S. M., Zingg, A., & Handy, M. (1987). The kinematics of movements along the Insubric Line and the emplacement of the Ivrea Zone. *Tectonophysics*, *135*(1-3), 47–66. https://doi.org/10.1016/0040-1951(87)90151-X

Schneider, S., Hammerschmidt, K., Rosenberg, C. L., Gerdes, A., Frei, D., & Bertrand, A. (2015). U–Pb ages of apatite in the western Tauern Window (Eastern Alps): Tracing the onset of collision-related exhumation in the European plate. *Earth and Planetary Science Letters*, *418*(Supplement C), 53–65. https://doi.org/10.1016/j.epsl.2015.02.020

Schönborn, G. (1999). Balancing cross sections with kinematic constraints: The Dolomites (northern Italy). *Tectonics*, *18*(3), 527–545. https://doi.org/10.1029/1998TC900018

Schorn, J. (1902). Die Erdbeben von Tirol und Vorarlberg. *Zeitschrift des Museum Ferdinandeum*, *III*(46), 99–282.

Schweizerischer Erdbebendienst (2010. Last update: 2011-03-15). Earthquake catalog ECOS-09. Retrieved from http://hitseddb.ethz.ch:8080/ecos09/index.html

Schweizerischer Erdbebendienst (2017). SED/ETH Realtime Regional Moment Tensors. Retrieved from http://www.seismo.ethz.ch/static/mti/

Selverstone, J. (1988). Evidence for east-west crustal extension in the Eastern Alps: implications for the unroofing history of the Tauern window. *Tectonics*, *7*(1), 87–105. https://doi.org/10.1029/TC007i001p00087

Singer, J., Diehl, T., Husen, S., Kissling, E., & Duretz, T. (2014). Alpine lithosphere slab rollback causing lower crustal seismicity in northern foreland. *Earth and Planetary Science Letters*, *397*(Supplement C), 42–56. https://doi.org/10.1016/j.epsl.2014.04.002

Slejko, D., Carulli, G. B., Carraro, F., Castaldini, D., Cavallin, A., Doglioni, C., et al. (1987). *Modello Sismotettonico dell`Italia Nord-Orientale*. Trieste: Consiglio Nazionale Delle Ricerce, Gruppo Nazionale per la Difesa dai Terremoti, Rendiconto n. 1.

Slejko, D., Carulli, G. B., Nicolich, R., Rebez, A., Zanferrari, A., Cavallin, A., et al. (1989). Seismotectonics of the eastern Southern Alps: A review. *Bollettino di Geofisica Teorica ed Applicata*, *31*(122), 109–136.

Slejko, D., & Rebez, A. (1988). Caratteristiche sismotettoniche dell'area benacense. Paper presented at 7° Convegno GNGTS, Roma.

Snoke, J. A. (1989). Earthquake mechanisms. In *Geophysics* (pp. 239–245). Boston, MA: Springer.

Snoke, J. A. (2003). FOCMEC: FOcal MEChanism determinations. In W. H. K. Lee, H. Kanamori, P. C. Jennings, & C. Kisslinger (Eds.), *International handbook of earthquake and engineering seismology*, *International Geophysics Series* (Vol. 81B, pp. 1629–1630). Amsterdam: Academic Press.

Spang, J. H. (1972). Numerical method for dynamic analysis of calcite twin lamellae. *Geological Society of America Bulletin*, *83*(2), 467–472. https://doi.org/10.1130/0016-7606(1972)83[467:NMFDAO]2.0.CO;2

Speranza, F., Minelli, L., Pignatelli, A., & Gilardi, M. (2016). Curie temperature depths in the Alps and the Po Plain (northern Italy): Comparison with heat flow and seismic tomography data. *Journal of Geodynamics*, *98*, 19–30. https://doi.org/10.1016/j.jog.2016.03.012

Sperner, B., & Ratschbacher, L. (1994). A turbo Pascal program package for graphical presentation and stress analysis of calcite deformation. *Zeitschrift der Deutschen Geologischen Gesellschaft*, *145*, 414–423.

Sperner, B., Ratschbacher, L., & Ott, R. (1993). Fault-striae analysis: A turbo pascal program package for graphical presentation and reduced stress-tensor calculation. *Computers & Geosciences*, *19*(9), 1361–1388. https://doi.org/10.1016/0098-3004(93)90035-4

Spiess, R. (1995). The Passeier-Jaufen Line: A tectonic boundary between Variscan and eo-Alpine Meran-Mauls basement. *Schweizerische Mineralogische und Petrographische Mitteilungen*, *75*(3), 413–425. https://doi.org/10.5169/seals-57165

Sprenger, W., & Heinisch, H. (1992). Late Oligocene to recent brittle transpressive deformation along the periadriatic lineament in the Lesach Valley (eastern Alps): Remote sensing and paleo stress analysis. *Annales Tectonicae*, *6*(2), 134–149.

Staufenberg, H. (1987). Apatite fission-track evidence for postmetamorphic uplift and cooling history of the eastern Tauern window and the surrounding Austroalpine (Central Eastern Alps, Austria). *Jahrbuch der Geologischen Bundesanstalt*, *130*(4), 571–586.

Stewart, J., & Watts, A. B. (1997). Gravity anomalies and spatial variations of flexural rigidity at mountain ranges. *Journal of Geophysical Research*, *102*(B3), 5327–5352. https://doi.org/10.1029/96JB03664

Töchterle, A., Brandner, R., & Reiter, F. (2011). Strain partitioning on major fault zones in the northwestern Tauern Window—Insights from the investigations to the Brenner Base Tunnel. *Austrian Journal of Earth Sciences*, *104*(1), 15–35.

TRANSALP Working Group, Gebrande, H., Lüschen, E., Bopp, M., Bleibinhaus, F., Lammerer, B., et al. (2002). First deep seismic reflection images of the Eastern Alps reveal giant crustal wedges and transcrustal ramps. *Geophysical Research Letters*, *29*(10), 1452. https://doi.org/10.1029/2002GL014911

Twiss, R. J., & Unruh, J. R. (1998). Analysis of fault slip inversions: Do they constrain stress or strain rate? *Journal of Geophysical Research*, *103*(B6), 12,205–12,222. https://doi.org/10.1029/98JB00612

van Gelder, I. E., Willingshofer, E., Sokoutis, D., & Cloetingh, S. A. P. L. (2017). The interplay between subduction and lateral extrusion: A case study for the European Eastern Alps based on analogue models. *Earth and Planetary Science Letters*, *472*, 82–94. https://doi.org/10.1016/j.epsl.2017.05.012

Vavryčuk, V. (2014). Iterative joint inversion for stress and fault orientations from focal mechanisms. *Geophysical Journal International*, *199*(1), 69–77. https://doi.org/10.1093/gji/ggu224

Viganò, A., Bressan, G., Ranalli, G., & Martin, S. (2008). Focal mechanism inversion in the Giudicarie–Lessini seismotectonic region (Southern Alps, Italy): Insights on tectonic stress and strain. *Tectonophysics*, *460*(1), 106–115. https://doi.org/10.1016/j.tecto.2008.07.008

Viganò, A., Scafidi, D., Ranalli, G., Martin, S., Della Vedova, B., & Spallarossa, D. (2015). Earthquake relocations, crustal rheology, and active deformation in the central–eastern Alps (N Italy). *Tectonophysics*, *661*, 81–98. https://doi.org/10.1016/j.tecto.2015.08.017

Viola, G., Mancktelow, N. S., & Seward, D. (2001). Late Oligocene-Neogene evolution of Europe-Adria collision: New structural and geochronological evidence from the Giudicarie fault system (Italian Eastern Alps). *Tectonics*, *20*(6), 999–1020. https://doi.org/10.1029/2001TC900021

Waldhauser, F., Lippitsch, R., Kissling, E., & Ansorge, J. (2002). High-resolution teleseismic tomography of upper-mantle structure using an a priori three-dimensional crustal model. *Geophysical Journal International*, *150*(2), 403–414. https://doi.org/10.1046/j.1365-246X.2002.01690.x

Wang, X., & Neubauer, F. (1998). Orogen-parallel strike-slip faults bordering metamorphic core complexes: The Salzach–Enns fault zone in the Eastern Alps, Austria. *Journal of Structural Geology*, *20*(6), 799–818. https://doi.org/10.1016/S0191-8141(98)00013-3

Willingshofer, E., & Cloetingh, S. (2003). Present-day lithospheric strength of the Eastern Alps and its relationship to neotectonics. *Tectonics*, *22*(6), 1075. https://doi.org/10.1029/2002TC001463

Wölfler, A., Dekant, C., Danišík, M., Kurz, W., Dunkl, I., Putiš, M., & Frisch, W. (2008). Late stage differential exhumation of crustal blocks in the central Eastern Alps: evidence from fission track and (U–Th)/He thermochronology. *Terra Nova*, *20*(5), 378–384. https://doi.org/10.1111/j.1365-3121.2008.00831.x

Wu, T. (2016). Draw focal mechanism beach balls as arcgis shapefile (Version 2.01, free script): ESRI ArcGIS code sharing. Retrieved from http://codesharing.arcgis.com/

Zang, A., & Stephansson, O. (2010). *Stress field of the Earth's crust*. New York: Springer.

Zattin, M., Cuman, A., Fantoni, R., Martin, S., Scotti, P., & Stefani, C. (2006). From Middle Jurassic heating to Neogene cooling: The thermochronological evolution of the southern Alps. *Tectonophysics*, *414*(1), 191–202. https://doi.org/10.1016/j.tecto.2005.10.020

Zentralanstalt für Meteorologie und Geophysik (2016. Last update: 2016-08-24). List of strong earthquakes in Austria (in German). Retrieved from https://www.zamg.ac.at/cms/de/geophysik/erdbeben/erdbeben-in-oesterreich/copy3_of_die-staerksten-erdbeben-in-oesterreich

Zoback, M. L. (1992). First- and second-order stress patterns in the lithosphere: the World Stress Map project. *Journal of Geophysical Research*, *97*(B8), 11703–11728. https://doi.org/10.1029/92JB00132

Zwingmann, H., & Mancktelow, N. S. (2004). Timing of Alpine fault gouges. *Earth and Planetary Science Letters*, *223*(3-4), 415–425. https://doi.org/10.1016/j.epsl.2004.04.041